IOP Publishing Modelling and Simulation in Materials Science and Engineering

Modelling Simul. Mater. Sci. Eng. **23** (2015) 085014 (37pp) doi:10.1088/0965-0393/23/8/085014

On mechanics and material length scales of failure in heterogeneous interfaces using a finite strain high performance solver

Matthew Mosby and Karel Matouš

Department of Aerospace and Mechanical Engineering, University of Notre Dame, Notre Dame, IN 46556, USA

E-mail: kmatous@nd.edu

Received 3 March 2015, revised 1 July 2015
Accepted for publication 7 August 2015
Published 26 October 2015

Abstract

Three-dimensional simulations capable of resolving the large range of spatial scales, from the failure-zone thickness up to the size of the representative unit cell, in damage mechanics problems of particle reinforced adhesives are presented. We show that resolving this wide range of scales in complex three-dimensional heterogeneous morphologies is essential in order to apprehend fracture characteristics, such as strength, fracture toughness and shape of the softening profile. Moreover, we show that computations that resolve essential physical length scales capture the particle size-effect in fracture toughness, for example. In the vein of image-based computational materials science, we construct statistically optimal unit cells containing hundreds to thousands of particles. We show that these statistically representative unit cells are capable of capturing the first- and second-order probability functions of a given data-source with better accuracy than traditional inclusion packing techniques. In order to accomplish these large computations, we use a parallel multiscale cohesive formulation and extend it to finite strains including damage mechanics. The high-performance parallel computational framework is executed on up to 1024 processing cores. A mesh convergence and a representative unit cell study are performed. Quantifying the complex damage patterns in simulations consisting of tens of millions of computational cells and millions of highly nonlinear equations requires data-mining the parallel simulations, and we propose two damage metrics to quantify the damage patterns. A detailed study of volume fraction and filler size on the macroscopic traction-separation response of heterogeneous adhesives is presented.

Keywords: multiscale cohesive modeling, computational homogenization, damage mechanics, high-performance computing, heterogeneous adhesives

(Some figures may appear in colour only in the online journal)

1. Introduction

Understanding of how materials fail is a long standing quest [1–22]. A crack has often been idealized as a separation of two adjacent material surfaces (two adjacent atomic layers) [1]. However, material failure is a result of massive breakage involving thousands of atomic planes localized to a representative zone that can be called the characteristic crack thickness, l_μ (see figure 1) [18, 23, 24]. Unfortunately, experimentally measuring this material length scale is extremely difficult. Recent theoretical work by Volokh [24–26] relates the volumetric and surface fracture energies to estimate the characteristic failure zone thickness, l_μ, of a material. Volokh shows that l_μ is $\mathcal{O}(10^0\ \mu\text{m})$ for typical metals, $\mathcal{O}(10^2\ \mu\text{m})$ for rubber, and $\mathcal{O}(10^4\ \mu\text{m})$ for concrete [24–26]. This knowledge of the failure zone is crucial in numerical modeling of damage since it introduces a length scale that must be numerically resolved for the physics of the problem to be captured.

Opposite to the characteristic length of damage localization, l_μ, is the macroscopic size of the structure, L of $\mathcal{O}(\text{m})$, and the size of a material domain that describes the material morphology with sufficient detail (i.e. Representative Unit Cell (RUC)), l_{RUC} of $\mathcal{O}(\text{mm})$, as shown in figure 1. Numerically resolving such a wide range of scales, $\mathcal{O}(10^3)$ from macro-to-micro (from m to mm) and $\mathcal{O}(10^3)$ from micro-to-l_μ (from mm to μm), is a challenge. This large range of scales usually results in simulations that are 2D [27], often within the small strain confines, and/or small strain 3D computations [28], but with small domains and discretizations unable to resolve the characteristic crack thickness. Therefore, obtaining in-depth understanding of the effects of material morphology on the fracture processes has traditionally been attempted through experiments [9, 10, 29–35]. However, to the best of our knowledge, a numerical study of damage that resolves the length scales from the failure zone, l_μ, up to the size of the RUC, l_{RUC}, in the 3D finite strains setting with complex material geometries has not been presented. Well resolved computations of this type can help address questions on the effect of particle volume fraction in the toughening response, the effect of particle diameter on non-monotonic fracture toughness, the competition between cohesive versus adhesive failure, and many others. Thus, performing such a three-dimensional study in the context of heterogeneous material interfaces is the aim of this work.

Heterogeneous interfaces are pervasive in engineering [29, 36, 37] as well as geological [38], biological [39], and many other natural and man-made applications. In engineering, typical examples are adhesive bonds replacing solder in electronics [36], dental adhesives [40], structural composite bonds [29], and bone repair adhesives [41]. In many of these examples, the heterogeneity is introduced to obtain desired mechanical properties or multi-functionality, such as in self-healing adhesives [37]. For instance, the addition of rubber particles to a stiffer epoxy increases fracture toughness due to cavitation and particle bridging [29]. The addition of glass particles to a softer adhesive increases fracture toughness by crack deflection and blunting [10]. Other constituents such as natural fibers [42] and carbon nanotubes [43] also modify mechanical properties, while the inclusion of silver flakes increases electrical conductivity [36]. Regardless of the reinforcement, the addition of these heterogeneities have a large effect on the macroscopic fracture response of the interface.

The multiscale cohesive modeling framework, proposed by Matouš *et al* [27], naturally includes the full description of the microscale in computing the overall macroscopic cohesive response. The multiscale cohesive theory is based on energy equivalence, i.e. Hill's Lemma [44], which introduces the concept of a RUC with in-plane dimension l_{RUC} and thickness of l_{c}. The dimension, l_{c}, corresponds to the actual thickness of the adhesive bond line, see figure 1. Following this work, there have been numerous studies of failure within heterogeneous interfaces in the 2D small strain setting [45–47]. The first 2D fully coupled multiscale

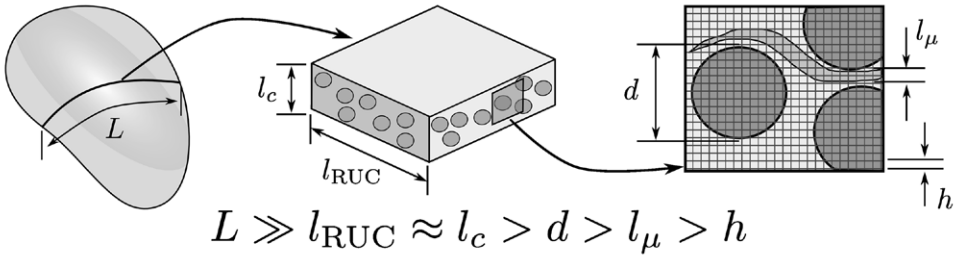

Figure 1. Multiscale modeling of failure in heterogeneous interfaces with widely varying spatial scales.

cohesive simulations of failure were published by Matouš' group in 2010 [48]. The original multiscale formulation for interfaces (Matouš *et al* [27]) was derived within the confines of small strains. Unfortunately, the small strain assumption is easily broken, especially at the micro-scale, even for a small macroscopic displacement jump across the cohesive surfaces. Therefore, Hirschberger *et al* [49] extended the formulation to finite strains, but did not consider material failure. The first fully coupled hyperelastic multiscale cohesive simulations in the 3D finite strain setting were presented by Mosby and Matouš [50]. Conen *et al* [51] presented a method to transition from bulk to cohesive multiscale modeling based on development of a strain localization band within the microstructure. McBride *et al* [52] added the effects of in-plane stretch and presented results in 3D. However, they did not include damage mechanics, and microscopic domains used in the numerical results included only one void or particle. Recently, Aragón *et al* [28] studied the effect of in-plane stretch on failure in 3D with domains containing 110 particles, but the formulation was in the small strain regime once more.

In this work, we use our in-house parallel 3D finite strains multiscale cohesive solver *PGFem3D* capable of capturing the large range of scales from l_μ to l_{RUC} (see figure 1). The primary focus of this work is to examine the link between material morphology and micro- and macro-scale damage response in complex three-dimensional microstructures. Specifically, we examine the discretization size (h) required to capture the characteristic crack thickness (l_μ), fracture toughness and strength, and the size of the RUC (l_{RUC}) that is required for macroscopically resolved and physically meaningful results. We also investigate the effect of particle volume fraction (c_{p}) and diameter (d) on the macroscopic cohesive response. Simulations involving this wide range of scales are inherently expensive, consisting of tens of millions of computational cells and millions of highly nonlinear equations, thus requiring the use of high-performance computing. Therefore, we employ a high-performance computational framework utilizing up to 1024 processing cores. We note that this parallel computing strategy is not the first of its kind (see e.g. [53]). However, executing such a framework is not a trivial task. We apply the parallel framework here, in the context of multiscale cohesive modeling of damage, to capture the wide range of spatial scales ($l_\mu \rightarrow l_{\mathrm{RUC}}$). These large simulations generate an enormous amount of data which is difficult to process for engineering decisions. Therefore, we use data-mining of the parallel simulations and introduce two damage metrics that allow us to characterize the damage pattern and quantify the effect of microstructure on the macroscopic cohesive characteristics, such as maximum traction (strength) and fracture toughness.

A key aspect of the multiscale modeling framework is development of a RUC. The size of a RUC for heterogeneous materials is related to both morphology and constituent material

properties (and their contrast), and is a frequent topic in computational material science [54–58]. While the literature is relatively rich with studies developing RUCs for hardening materials, there are comparatively fewer studies for materials with softening [55, 56]. Kulkarni *et al* [45] performed a RUC size study based on the convergence of mean and standard deviation of failure response in a thin heterogeneous interface. In Kulkarni *et al* [45], cells were generated by Random Sequential Addition (RSA) and showed fast convergence of mean response, but very slow convergence of the standard deviation.

This work follows the concept of data-driven (image-based) modeling, and we propose to reconstruct RUCs from statistics of a material sample, similarly to our prior work on bulk materials [57, 59]. In this way, our unit cells not only match particle size and volume fraction, but overall second-order statistical description. We show that using a statistically equivalent RUC leads to more accurate and faster convergence of response with respect to the cell size.

The paper is organized as follows: section 2 provides the finite strain multiscale cohesive modeling formulation. Section 3 describes the method for reconstructing RUCs from statistical material data. Section 4 presents the numerical results and analysis of the multiscale studies. Finally, conclusions are drawn in section 5.

2. Governing equations

In this section, we present the 3D finite strain multiscale cohesive formulation. Our work is based on the original small strains model derived by Matouš *et al* [27] that was extended to finite strains by Hirschberger *et al* [49]. Here we extend the 3D finite strain multiscale cohesive model to include damage mechanics, and implement it in a highly parallel computing environment. In the following subsections, we provide an overview of the finite strain multiscale kinematics, the scale transition using the Hill–Mandel condition for interfaces, and the constitutive failure response at the microscale. Our computational work makes use of finite element procedures implemented for parallel computing, and the interested reader is referred to appendix A for details of the computational implementation.

2.1. Macroscale problem

Consider a body $\Omega_0 \subset \mathbb{R}^3$ consisting of material points $\boldsymbol{X} \in \Omega_0$ (see figure 2). The boundary $\partial\Omega_0$ is decomposed such that $\partial\Omega_0 = \partial\Omega_0^u \cup \partial\Omega_0^t$ and $\partial\Omega_0^u \cap \partial\Omega_0^t = \varnothing$. Let the boundaries $\partial\Omega_0^u$ and $\partial\Omega_0^t$ represent the areas of applied displacement $\bar{\boldsymbol{u}}$ and traction $\bar{\boldsymbol{t}}$, respectively. Next, let the adhesive layer with thickness $l_c > 0$ be represented by an oriented manifold $\Gamma_0 \in \mathbb{R}^2$ with unit normal ${}^0\boldsymbol{N}(\boldsymbol{X})$ in the reference configuration. The manifold decomposes Ω_0 into two bodies (adherends) denoted by Ω_0^+ and Ω_0^-. The deformation of the adherends is described by the deformation map and its gradient

$$\begin{aligned} {}^0\boldsymbol{\varphi}(\boldsymbol{X}) &= \boldsymbol{X} + {}^0\boldsymbol{u}(\boldsymbol{X}) && \forall\, \boldsymbol{X} \in \Omega_0^{\pm}, \\ {}^0\boldsymbol{F}(\boldsymbol{X}) &= \nabla_{\boldsymbol{X}}\, {}^0\boldsymbol{\varphi} = \mathbf{1} + \nabla_{\boldsymbol{X}}\, {}^0\boldsymbol{u} && \forall\, \boldsymbol{X} \in \Omega_0^{\pm}, \end{aligned} \tag{1}$$

where $\mathbf{1}$ is the second-order identity tensor, and ${}^0\boldsymbol{u}(\boldsymbol{X})$ is the macroscale displacement. Under arbitrary loading, there is a jump in the deformation across the interface,

$$[\![\, {}^0\boldsymbol{\varphi} \,]\!](\boldsymbol{X}) = {}^0\boldsymbol{\varphi}^+(\boldsymbol{X}) - {}^0\boldsymbol{\varphi}^-(\boldsymbol{X}) = [\![\, {}^0\boldsymbol{u} \,]\!](\boldsymbol{X}) \quad \forall\, \boldsymbol{X} \in \Gamma_0, \tag{2}$$

and we define the average deformation gradient as

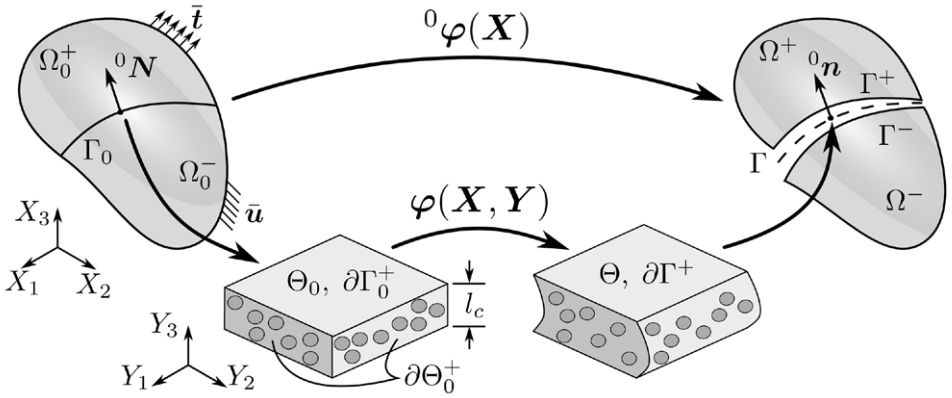

Figure 2. Kinematics of multiscale cohesive modeling. Note that Ω_0 represents the macro-domain, while Θ_0 is the micro-domain.

$$ {}^0\boldsymbol{F}(\boldsymbol{X}) = \boldsymbol{1} + \frac{1}{l_c}[\![{}^0\boldsymbol{u}]\!](\boldsymbol{X}) \otimes {}^0\boldsymbol{N}(\boldsymbol{X}) \quad \forall\, \boldsymbol{X} \in \Gamma_0. \tag{3} $$

Neglecting inertial forces, the macroscale equilibrium boundary value problem is given by

$$ \begin{aligned} \nabla_{\boldsymbol{X}} \cdot {}^0(\boldsymbol{FS}) + \boldsymbol{b}_0 &= \boldsymbol{0} && \in \Omega_0^{\pm}, \\ {}^0(\boldsymbol{FS}) \cdot {}^0\boldsymbol{N} &= \bar{\boldsymbol{t}} && \text{on } \partial\Omega_0^t, \\ {}^0\boldsymbol{u} &= \bar{\boldsymbol{u}} && \text{on } \partial\Omega_0^u, \\ {}^0\boldsymbol{t}^+ + {}^0\boldsymbol{t}^- &= \boldsymbol{0} && \text{on } \Gamma_0, \end{aligned} \tag{4} $$

where ${}^0\boldsymbol{S} = 2\partial {}^0W/\partial {}^0\boldsymbol{C}$ is the macroscopic second Piola-Kirchhoff stress tensor, ${}^0\boldsymbol{C} = {}^0\boldsymbol{F}^{\mathrm{T}}\,{}^0\boldsymbol{F}$ is the macroscopic right Cauchy-Green deformation tensor, and ${}^0W$ is any suitable, e.g. hyperelastic, macroscopic strain energy density function. Application of standard variational procedures leads to the weak form of the boundary value problem given in equation (4). Find ${}^0\boldsymbol{u}(\boldsymbol{X}) \in \mathscr{C}_{\Omega_0}\left\{ {}^0\boldsymbol{u} : \Omega_0 \to \mathbb{R}^3 |\ \det({}^0\boldsymbol{F}) > 0 \text{ in } \Omega_0 \text{ and } {}^0\boldsymbol{u}|_{\partial\Omega_0^u} = \bar{\boldsymbol{u}} \right\}$ such that

$$ \begin{aligned} R_{{}^0\boldsymbol{u}} := & \int_{\Omega_0^{\pm}} {}^0\boldsymbol{S} : [{}^0\boldsymbol{F}^{\mathrm{T}} \nabla_{\boldsymbol{X}} \delta\, {}^0\boldsymbol{u}]^{\mathrm{sym}}\, \mathrm{d}V + \int_{\Gamma_0} {}^0\boldsymbol{t} \cdot [\![\delta\, {}^0\boldsymbol{u}]\!]\, \mathrm{d}A \\ & - \int_{\Omega_0^t} \bar{\boldsymbol{t}} \cdot \delta\, {}^0\boldsymbol{u}\, \mathrm{d}A - \int_{\Omega_0^{\pm}} \boldsymbol{b}_0 \cdot \delta\, {}^0\boldsymbol{u}\, \mathrm{d}V = 0 \end{aligned} \tag{5} $$

holds for variations $\delta\, {}^0\boldsymbol{u}(\boldsymbol{X}) \in \mathscr{V}_{\Omega_0}\{\delta\, {}^0\boldsymbol{u} : \Omega_0 \to \mathbb{R}^3 |\ \delta\, {}^0\boldsymbol{u}|_{\partial\Omega_0^u} = \boldsymbol{0}\}$. Equation (5) is identical to the classical cohesive modeling formulation [4]. Note that in traditional cohesive modeling, ${}^0\boldsymbol{t}$ is defined by a phenomenological traction-separation relation [4, 5]. In this work, the traction-separation relation is computationally derived from the microscale response as described in the following sections.

2.2. Microscale problem

A microstructure $\Theta_0 \subset \mathbb{R}^3$ consisting of microscale points $\boldsymbol{Y} \in \Theta_0$ is locally attached to each macroscale point $\boldsymbol{X} \in \Gamma_0$ (see figure 2). The motion and deformation gradient in the microstructure are functions of both macro- and micro-variables as

$$\begin{aligned} \boldsymbol{\varphi}(\boldsymbol{X},\boldsymbol{Y}) &= {}^0\boldsymbol{F}(\boldsymbol{X})\boldsymbol{Y} + {}^1\boldsymbol{u}(\boldsymbol{Y}) \qquad \forall\, \boldsymbol{Y} \in \Theta_0, \\ \boldsymbol{F}(\boldsymbol{X},\boldsymbol{Y}) &= {}^0\boldsymbol{F}(\boldsymbol{X}) + \nabla_{\boldsymbol{Y}}\, {}^1\boldsymbol{u}(\boldsymbol{Y}) \qquad \forall\, \boldsymbol{Y} \in \Theta_0, \end{aligned} \tag{6}$$

where ${}^1\boldsymbol{u}(\boldsymbol{Y})$ is the microscale displacement fluctuations. The boundary, $\partial\Theta_0$, is decomposed into non-overlapping sections $\partial\Theta_0^{\pm}$ and $\partial\Gamma_0^{\pm}$ corresponding to the $Y_{1,2}^{\pm}$ and $Y_3^{\pm}$ faces respectively (see bottom left of figure 2). In this work, Θ_0 is $Y_{1,2}$-periodic. The microscale equilibrium boundary value problem, neglecting body forces and without prescribed traction, is given by

$$\nabla_{\boldsymbol{Y}} \cdot (\boldsymbol{F}\,{}^1\boldsymbol{S}) = \boldsymbol{0} \quad \in \Theta_0, \quad \text{with} \quad \boldsymbol{\varphi} = \overline{\boldsymbol{\varphi}} \quad \text{on } \partial\Theta_0. \tag{7}$$

In equation (7), $\overline{\boldsymbol{\varphi}}(\boldsymbol{X},\boldsymbol{Y})$ is a prescribed motion, ${}^1\boldsymbol{S} = 2\partial {}^1W/\partial \boldsymbol{C}$ is the microscale second Piola-Kirchhoff stress, and $\boldsymbol{C} = \boldsymbol{F}^{\mathrm{T}}\boldsymbol{F}$. We will describe the form of ${}^1W$, the microscale strain energy density function, in section 2.4. The weak form of equation (7) is derived from the micro-to-macro transition with a particular set of physically applicable and mathematically admissible boundary conditions. The micro-to-macro transition is described in the next section.

2.3. Micro-to-macro transition

In computational homogenization, the behavior of a material point at the macroscale is linked to the microscale through the Hill–Mandel stationarity condition [44], and for interfaces [27, 49] is given by

$$\inf_{[\![{}^0\boldsymbol{u}]\!]} {}^0\psi([\![{}^0\boldsymbol{u}]\!]) = \inf_{[\![{}^0\boldsymbol{u}]\!]} \inf_{{}^1\boldsymbol{u}} \frac{l_{\mathrm{c}}}{|\Theta_0|} \int_{\Theta_0} {}^1W({}^0\boldsymbol{F} + \nabla_{\boldsymbol{Y}}\, {}^1\boldsymbol{u})\, \mathrm{d}\Theta, \tag{8}$$

which minimizes the potential energy at both scales. Equation (8) relates the macroscopic traction potential energy, ${}^0\psi$, to the average of the microscale strain energy density, ${}^1W$. Note that the formulation departs from the bulk homogenization in that l_{c} scales the volume average microscale strain energy in order to equate it to the macroscale traction potential.

The Hill–Mandel condition places restrictions on the microscale kinematics [44], equation (6), namely

$$\frac{1}{|\Theta_0|} \int_{\Theta_0} \nabla_{\boldsymbol{Y}} {}^1\boldsymbol{u}\, \mathrm{d}\Theta = \frac{1}{|\Theta_0|} \int_{\partial\Theta_0} {}^1\boldsymbol{u} \otimes \boldsymbol{N}\, \mathrm{d}A = \boldsymbol{0}, \tag{9}$$

where $\boldsymbol{N}$ is the unit normal to $\partial\Theta_0$. For multiscale modeling of heterogeneous layers, we use hybrid (semi-periodic) boundary conditions [27, 49] given by

$${}^1\boldsymbol{u} = \boldsymbol{0} \text{ on } \partial\Gamma_0^{\pm}, \quad {}^1\boldsymbol{u}^+ - {}^1\boldsymbol{u}^- = \boldsymbol{0} \text{ on } \partial\Theta_0^{\pm}, \quad {}^1\boldsymbol{t}^+ + {}^1\boldsymbol{t}^- = \boldsymbol{0} \text{ on } \partial\Theta_0^{\pm}, \tag{10}$$

where $\partial\Gamma_0^{\pm}$ are the top and bottom surfaces of the layer, and $\partial\Theta_0^{\pm}$ are positive and negative Y_1 (front and back) and Y_2 (right and left) faces of the cell, respectively. The hybrid boundary conditions (shown schematically in figure 3) are physically motivated by fixing the top and bottom surfaces of the adhesive layer, $\partial\Gamma_0^{\pm}$, to the adherends, and approximating an infinite medium in the $Y_{1,\,2}$-directions, $\partial\Theta_0^{\pm}$ (see equation (10)). Admissibility of the hybrid boundary conditions are proved in [27, 49]. We note that other mathematically admissible boundary conditions are also physically applicable to multiscale modeling of heterogeneous layers, such as homogeneous kinematic boundary conditions (${}^1\boldsymbol{u} = \boldsymbol{0}$ on $\partial\Theta_0$) or the Taylor model (${}^1\boldsymbol{u} = \boldsymbol{0}\ \forall\, \boldsymbol{Y} \in \Theta_0$). In the case of a homogeneous layer, the hybrid and homogeneous

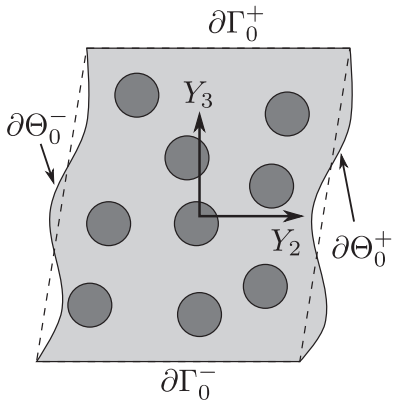

Figure 3. The hybrid (semi-periodic) boundary conditions on $\partial\Theta_0$.

kinematic boundary conditions yield identical response to the Taylor model. We will return to this point in section 4.3.

We now derive the weak form of the microscale equilibrium (equation (7)). Taking variations of equation (8) with respect to ${}^1\boldsymbol{u}$, we arrive at the weak form of the microscale problem. Find ${}^1\boldsymbol{u}(\boldsymbol{Y}) \in \mathscr{C}_{\Theta_0}\left\{ {}^1\boldsymbol{u} : \Theta_0 \to \mathbb{R}^3 | \det(\boldsymbol{F}) > 0 \text{ in } \Theta_0,\ {}^1\boldsymbol{u}|_{\partial\Gamma_0^\pm} = \boldsymbol{0} \text{ and } {}^1\boldsymbol{u} \text{ is } Y_{1,2}-\text{periodic on } \partial\Theta_0^\pm \right\}$ such that

$$\mathscr{R}_{{}^1\boldsymbol{u}} := \frac{l_c}{|\Theta_0|}\int_{\Theta_0} {}^1\boldsymbol{S} : [\boldsymbol{F}^{\mathrm{T}}\nabla_{\boldsymbol{Y}}\delta\,{}^1\boldsymbol{u}]^{\mathrm{sym}}\,\mathrm{d}\Theta = 0 \tag{11}$$

holds for variations $\delta\,{}^1\boldsymbol{u}(\boldsymbol{Y}) \in \mathscr{V}_{\Theta_0}\{\delta\,{}^1\boldsymbol{u} : \Theta_0 \to \mathbb{R}^3 |\ \delta\,{}^1\boldsymbol{u}|_{\partial\Gamma_0^\pm} = \boldsymbol{0} \text{ and } \delta\,{}^1\boldsymbol{u} \text{ is } Y_{1,2}-\text{periodic on } \partial\Theta_0^\pm\}$. Note that the macroscopic constitutive response of the interface is given by

$${}^0\boldsymbol{t} = \frac{\partial\,{}^0\psi}{\partial[\![\,{}^0\boldsymbol{u}]\!]}, \tag{12}$$

which is the result of Coleman and Noll's procedure [60, 61]. Taking the variation of equation (8) with respect to $[\![\,{}^0\boldsymbol{u}]\!]$ yields

$$\mathscr{R}_{[\![{}^0\boldsymbol{u}]\!]} := \left[\frac{1}{|\Theta_0|}\left\{\int_{\Theta_0} \boldsymbol{F}\ {}^1\boldsymbol{S}\,\mathrm{d}\Theta\right\}\cdot{}^0\boldsymbol{N} - {}^0\boldsymbol{t}\right]\cdot[\![\delta\,{}^0\boldsymbol{u}]\!] = 0, \tag{13}$$

where $\delta\,{}^0\boldsymbol{u}(\boldsymbol{X}) \in \mathscr{V}_{\Omega_0}$. Upon microscale equilibrium, equation (13) yields the closure on the macroscale traction, namely

$${}^0\boldsymbol{t} = \frac{1}{|\Theta_0|}\left[\int_{\Theta_0} \boldsymbol{F}\ {}^1\boldsymbol{S}\,\mathrm{d}\Theta\right]\cdot{}^0\boldsymbol{N}, \tag{14}$$

and is used at the macroscale in equation (5).

2.4. Microscale constitutive model

Concern of the multiscale formulation is now turned to definition of a constitutive model at the microscale. We use an isotropic viscous damage model based on irreversible thermodynamics

and internal state variables theory as described in [12, 13, 27, 45, 48]. For completeness of the presentation, we summarize the damage model in what follows.

Consider the strain energy density function from equation (8)

$$^1W(\boldsymbol{C},\omega) = (1-\omega)\,{}^1\overline{W}(\boldsymbol{C}), \tag{15}$$

where $\omega \in [0,1]$ is the isotropic damage variable. In this work, we use the Neo-Hookean hyperelastic model and employ the volumetric and deviatoric split, ${}^1\overline{W}(\boldsymbol{C}) = {}^1\overline{W}(\hat{\boldsymbol{C}}) + {}^1\overline{U}(J)$, with

$$\begin{aligned} {}^1\overline{W}(\hat{\boldsymbol{C}}) &= \frac{\mu^*}{2}[\mathrm{tr}(\hat{\boldsymbol{C}}) - 3], \\ {}^1\overline{U}(J) &= \frac{\kappa}{2}[\exp(J-1) - \ln(J) - 1]. \end{aligned} \tag{16}$$

In equation (16), $J = \det(\boldsymbol{F})$ is the Jacobian of the deformation, $\hat{\boldsymbol{C}} = J^{-2/3}\boldsymbol{C}$ is the deviatoric right Cauchy-Green deformation tensor, μ^* is the shear modulus, and κ is the bulk modulus. The Clausius–Duhem inequality, neglecting all but mechanical effects, reads

$$-{}^1\dot{W} + \frac{1}{2}{}^1\boldsymbol{S} : \dot{\boldsymbol{C}} \geqslant 0, \tag{17}$$

where $(\dot{\bullet})$ denotes the material time derivative. Substituting for ${}^1\dot{W}$ and using standard arguments of thermodynamics yields

$${}^1\boldsymbol{S} = (1-\omega)\,2\frac{\partial {}^1\overline{W}}{\partial \boldsymbol{C}} \quad \text{and} \quad \mathscr{D}^{\omega} := -\dot{\omega}Y \geqslant 0, \tag{18}$$

where $\mathscr{D}^{\omega}$ is the damage dissipation, and $-Y = \overline{Y} = {}^1\overline{W}$ is the damage energy release rate, thermodynamic force conjugate to the damage variable, ω. The evolution of damage is governed by a damage surface analogous to a yield surface in plasticity [12, 13],

$$g(\overline{Y}, \chi^t) = G(\overline{Y}) - \chi^t \leqslant 0, \tag{19}$$

where $G(\overline{Y})$ is a function describing the damage process in the material and χ^t, $\chi^{t=0} = 0$, is the damage internal state variable which describes the maximum damage reached at a given material point. The damage process is governed by

$$\dot{\omega} = \dot{\lambda}\frac{\partial g}{\partial \overline{Y}} = \dot{\lambda}H, \quad \dot{\chi}^t = \dot{\lambda}H, \quad \chi^t = \max\left\{\chi^0, \max_{s\in(-\infty,t]}\chi^s\right\}, \tag{20}$$

where $H = \partial G/\partial\overline{Y}$ and $\dot{\lambda} = \dot{\overline{Y}}$ is the damage consistency parameter. We assume unloading towards the origin. The damage loading/unloading is governed by the Kuhn–Tucker consistency conditions:

$$\dot{\lambda} \geqslant 0, \quad g(\overline{Y}, \chi^t) \leqslant 0, \quad \dot{\lambda}g(\overline{Y}, \chi^t) = 0. \tag{21}$$

It has been shown that many adhesives exhibit a range of viscous behavior [62, 63]. Therefore, we employ a linear viscous damage model as in [12, 13, 27, 45, 48], which reformulates the evolution equation (20) as

$$\dot{\omega} = \dot{\lambda}H \rightarrow \dot{\omega} = \mu\langle g\rangle \quad \text{and} \quad \dot{\chi}^t = \dot{\lambda}H \rightarrow \dot{\chi}^t = \mu\langle g\rangle, \tag{22}$$

where $\mu \in [0,\infty)$ [s^{-1}] is a damage viscosity parameter and $\langle\bullet\rangle$ are McAuley brackets. The damage viscosity is inverse proportionally related to the damage relaxation time, $\mu \propto 1/\tau$. Voyiadjis [11] suggested that for certain materials and loading rates, the damage viscosity (μ) can be assumed as proportionally related to material (extensional) viscosity, η [Pa·s],

by $\mu \propto E/\eta$ where E is Young's modulus. This introduces a viscous damage length scale $l_\mu \propto \eta/\sqrt{E\rho} \propto E/\left(\mu\sqrt{E\rho}\right)$, where ρ is the material density and $\sqrt{E\rho}$ is the longitudinal wave propagation speed. We note that the viscous damage model has its own limitations and the localization zone, l_μ, can be introduced using different theories, e.g. non-local damage models [8]. Nevertheless, we use a viscous damage model in this work for simplicity of implementation. However, we attempt to calibrate the damage viscosity such that it lies within the range of material data. Thus, we relate μ to the characteristic damage length scale [24, 25], l_μ, in order to capture the physical behavior of interest (e.g. particle size effect). A value of $\mu = 0$ gives the instantaneous hyperelastic response while $\mu \to \infty$ recovers the rate-independent damage model. Finally, we note that the damage viscosity also regularizes the solution of the governing boundary value problem, equation (7), which retains the strong material ellipticity [12, 13].

In this work, the Weibull function,

$$G(\overline{Y}) = 1 - \exp\left[-\left(\frac{\overline{Y} - Y_{\text{in}}}{p_1 Y_{\text{in}}}\right)^{p_2}\right], \tag{23}$$

is used to describe the damage process for $\overline{Y} > Y_{\text{in}}$, where p_1, p_2 and Y_{in} are material parameters denoting scale, shape, and initial damage energy threshold respectively. We discuss the values of the damage parameters in section 4. Note that the damage surface, equation (19), and the three parameter isotropic damage function, equation (23), govern the character of the normal versus shear material strength and fracture toughness. Moreover, the finite strain kinematics couple all loading modes. We will comment on this further in section 4. The computational implementation of the isotropic damage model based on an adaptive time-stepping scheme is presented in appendix B.

3. Statistical characterization and representative unit cell reconstruction

In this section, we extend the statistical characterization and unit cell reconstruction techniques developed for bulk materials in [57, 59] to material layers. We use our software tools for statistical characterization, *Stat3D*, and reconstruction, *Recon3D*, that both run in a parallel computing environment [57, 59]. The material characterization and cell reconstruction results were computed on up to 1024 processing cores.

In data-driven (image-based) modeling, the material morphology is typically obtained from experiments such as micro-computed tomography, or scanning electron microscopy, etc [64]. Other possible data sources are digital microstructures obtained from packing algorithms such RSA, or the Lubachevsky-Stillinger packing algorithm [65], just to name a few. Regardless of its source (experimental and/or digital), this large volume of morphological data lends itself to statistical characterization. In our work, we use the isotropic one- and two-point probability functions [58],

$$S_r(\boldsymbol{Y}) = c_r, \quad \text{and} \quad S_{rs}(\boldsymbol{Y}, \boldsymbol{Y}') = S_{rs}(\|\boldsymbol{Y} - \boldsymbol{Y}'\|). \tag{24}$$

In equation (24), c_r is the volume fraction of phase r and S_{rs} is the probability of the endpoints of a line of length $l = \|\boldsymbol{Y} - \boldsymbol{Y}'\|$ existing in both phases r and s simultaneously. For bulk materials, all orientations of the line in 3D space are averaged to obtain the isotropic second-order statistical representation. For material layers of a given thickness, l_c, we propose in-plane material sampling, i.e. only horizontal orientations of the random line, l, in 3D space are averaged. Nevertheless, the full 3D character of the material is preserved since the

sampling proceeds randomly throughout the thickness of the layer (l_c). Thus, the functions S_{rs} are in-plane isotropic. The saturation of S_{rs} yields a geometric length scale, l_{stat}, which is the smallest sample that can statistically describe the overall material. The saturation point used to determine l_{stat} is given by the point at which derivatives of all in-plane isotropic two-point probability functions reach zero.

In this work, we digitally generate material samples by RSA. We call these digital samples packs. For each material mixture, five random packs are generated and statistically characterized. Figure 4(a) shows one pack with 10% volume fraction of 20 μm diameter particles and overall dimensions of $1000 \times 1000 \times 200$ μm^3, containing 4774 particles. Figure 4(b) shows the average in-plane isotropic two-point probability functions for the five packs. The maximum standard deviation for all functions is $2.79 \cdot 10^{-4}$, and error bars representing one standard deviation are not shown since they are small in this case. The geometric length scale for this material is $l_{stat} = 2l = 140$ μm, and is denoted by the dashed vertical line in figure 4(b).

The geometry of the cell with dimensions $l_{cell} \times l_{cell} \times l_c$ is reconstructed using a genetic algorithm [59]. For completeness, we provide a brief description of the reconstruction procedure augmented in this work for material layers. Using an initial guess for the side length of the cell, typically l_{stat}, the least-square difference of the one-point probability functions (volume fraction) is minimized. The first objective function for spherical mono-disperse particle mixtures is given by

$$\mathcal{F}_1(l_{cell}) = \sqrt{(c_p - c_c)^2} = \sqrt{\left(c_p - \frac{4\pi r^3 n}{3 l_c l_{cell}^2}\right)^2}, \tag{25}$$

where c_p and c_c are the volume fractions of particles in the pack and the cell, respectively. The number of particles is denoted by n, and r is the radius of the particles. Note that the extension of this objective function to poly-disperse packs is trivial (see [59]). The optimal size of the cell is determined analytically from the local minimum of equation (25):

$$\frac{d\mathcal{F}_1}{dl_{cell}} = 0 \Rightarrow l_{cell} = \sqrt{\frac{4\pi n r^3}{3 l_c c_p}}. \tag{26}$$

After optimizing the size of the cell, the in-plane isotropic two-point probability functions are matched to find the optimal location of particle centers. The second objective function minimizes the L_2 error of the in-plane isotropic statistics between the pack and cell and reads

$$\mathcal{F}_2(\boldsymbol{Y}_n) = \sum_r^N \sum_s^N \|S_{rs}^p - S_{rs}^c\|_{L^2}, \tag{27}$$

where $\boldsymbol{Y}_n$ are the positions of the particles in the cell. Note that our cells are $Y_{1,2}$-periodic (see section 2.3 regarding the hybrid boundary conditions). More details on the reconstruction procedure are given in [57, 59].

For the RUC convergence study presented in section 4.2, we reconstruct five cells each with side lengths given by $l_{cell} \approx 1/2\, l_{stat}$, $l_{cell} \approx l_{stat}$, and $l_{cell} \approx 2\, l_{stat}$ (69.408, 139.569, and 279.887 μm) containing 10% volume fraction of 20 μm diameter particles. Figure 5(a) shows a comparison between the pack and a cell with $l_{cell} \approx l_{stat}$. Figure 5(b) shows a comparison of average in-plane isotropic two-point probability functions from the pack and cells with different side lengths. The standard deviations are very small and are not shown. The maximum standard deviation of all functions for all reconstructed cells is $8.65 \cdot 10^{-4}$.

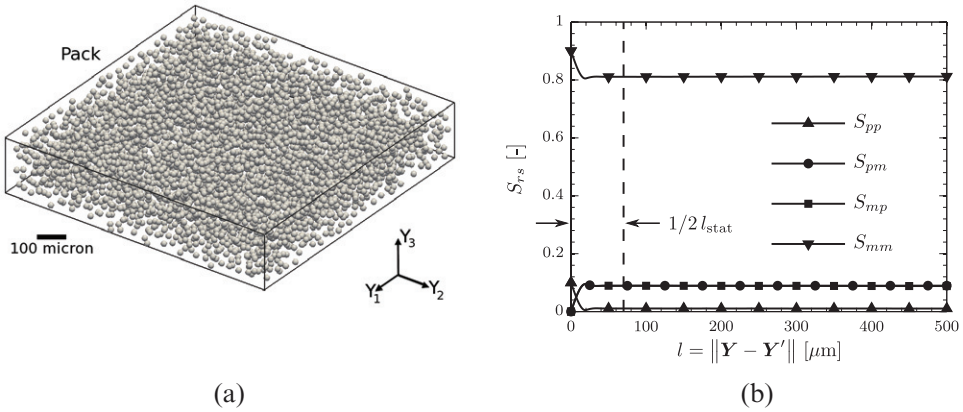

Figure 4. A random material pack and in-plane isotropic two-point probability functions. (a) A pack consisting of 10% volume fraction of 20 μm diameter particles ($1000 \times 1000 \times 200$ μm^3 with 4774 particles). (b) Average in-plane isotropic two-point probability functions (S_{rs}) for five realizations of the pack (p - particle, m - matrix). The vertical dashed line that defines $1/2\, l_{\text{stat}}$ (the saturation point) is determined by the point at which derivatives of all S_{rs} functions reach zero.

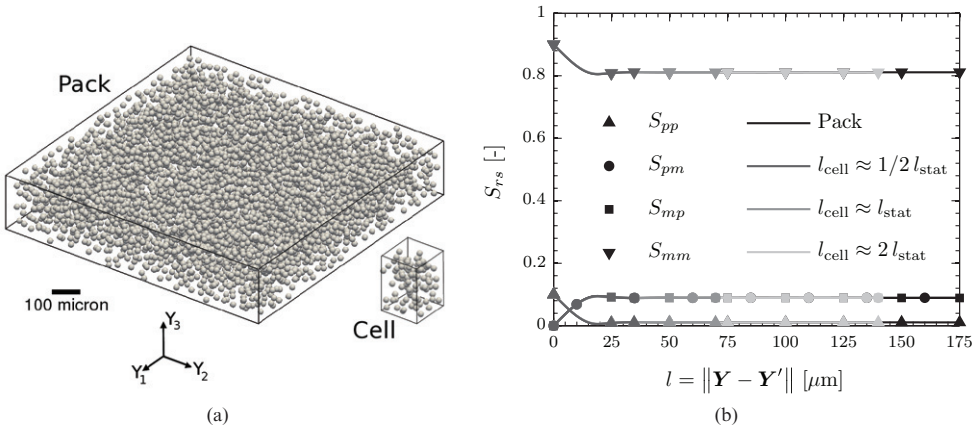

Figure 5. Comparison of morphology and average statistical functions for the pack and its statistically equivalent $Y_{1,2}$-periodic cells containing 10% volume fraction of 20 μm diameter particles. (a) Comparison between the pack (4774 particles in $1000 \times 1000 \times 200$ μm^3) and the cell with $l_{\text{cell}} \approx l_{\text{stat}}$ (93 particles in $139.569 \times 139.569 \times 200$ μm^3). (b) Comparison of the average in-plane isotropic two-point probability functions from the different cells and the pack. Markers denote different probability functions, and gray-scale denotes cells with different side lengths. The subscripts p and m denote particle and matrix phases, respectively.

Note that all of the different sized cells accurately capture the statistics due to the reconstruction algorithm.

In order to determine the relative accuracy of different cell generation methods, we compute the statistics of five cells generated by RSA with $l_{\text{cell}} = 139.569$ μm and compare them to those from the reconstructed cells. A comparison of the average L_2 error with respect to the pack, using equation (27), and the maximum standard deviation for all in-plane isotropic probability functions is shown in table 1. Both cell generation methods have similar precision (indicated

Table 1. Average L_2 error and maximum standard deviation of two-point isotropic probability functions for RSA generated and statistically optimal cells with $l_{\text{cell}} = 139.569\ \mu$m.

	Avg. L_2 error	Max. std. dev.
RSA	0.0778 ± 0.0069	0.0011
Statistically optimal	0.0112 ± 0.0023	0.0008

by similar maximum standard deviations), but the statistically optimal cells capture the pack statistics approximately seven times better. While the link between morphology, statistics, and the overall material behavior is complex, it has been shown that even small variations in statistics can have a significant effect on macroscopic properties [64]. Thus, cells which match the statistics of the overall material morphology as closely as possible are preferred.

In this section, we have presented a method for characterization of material layers (packs) and reconstruction of statistically optimal unit cells within the context of image-based modeling. The statistically optimal cells provide a more accurate and precise representation (in the L_2 sense) of the material morphology than typical material-blind packing algorithms (e.g. RSA). In addition to accurately representing the material geometry, RUCs must also provide accurate physical response. In section 4.2, we examine the link between the geometric length scale, l_{stat}, and the physical size of a RUC, l_{RUC}, required to yield representative macroscopic response.

4. Numerical results

The following section details the numerical studies performed for the physical analysis. First, the required mesh size is determined from a grid convergence study. Then, the required size of a RUC with respect to the statistical length scale is determined by a convergence study of physical behavior. For both of these studies, the adhesive layer consists of 10% volume fraction of 20 μm diameter particles. After determining the required mesh and RUC size, analysis of the effects of particle volume fraction and diameter on the multiscale response of the adhesive layer is presented.

In this work, we are interested in complex loading conditions where all three fracture modes are present (mode I, normal opening; mode II, in-plane shear; mode III, out-of-plane shear). Therefore, the mixed-mode macroscopic loading history, with $[\![{}^0u_1]\!] = [\![{}^0u_2]\!] = [\![{}^0u_3]\!]$ and a macroscopic loading rate of $\|[\![{}^0\dot{\boldsymbol{u}}]\!]/l_c\| = 0.1\ \text{s}^{-1}$ is used for all examples. Note that we do not solve the fully coupled multiscale problem in this work. Fully coupled cohesive multiscale simulations of damage in 2D and hyperelasticity in 3D were presented in [48] and [50], respectively. Instead, we prescribe the macroscale deformation gradient, equation (3), and solve the microscale problem given by equation (11). Upon equilibrium, the macroscopic traction vector is evaluated using equation (14). The solution is obtained using our multiscale parallel solver, *PGFem3D* [66, 67], executed on up to 512 processing cores. See appendix A for details regarding the parallel computational implementation. Under the prescribed loading conditions, and due to isotropy of the RUCs (in the $Y_{1,2}$-direction), the traction-separation response in the $Y_{1,2}$-directions is identical for the purposes of engineering analysis. For simplicity of presentation, we reduce results to the normal and shear directions defined as

$$(\bullet)_n = (\bullet)_3 \quad \text{and} \quad (\bullet)_s = \sqrt{(\bullet)_1^2 + (\bullet)_2^2}, \tag{28}$$

where $(\bullet)_i$ is the i-th component of ${}^0\boldsymbol{t}$ or $[\![{}^0\boldsymbol{u}]\!]$, respectively.

Table 2. Constituent material properties for the adhesive layer.

	E [MPa]	ν [-]	Y_{in} [MPa]	p_1 [-]	p_2 [-]	μ [s^{-1}]
Particle	2.4e3	0.34	0.32	2.5	8.0	100.0
Matrix	8.0e2	0.34	0.15	8.0	2.5	100.0

Note: E and ν are Young's modulus and Poisson's ratio, respectively. The damage model is governed by the initial damage energy threshold, Y_{in}, the scale and shape parameters of the damage function, p_1 and p_2, and the damage viscosity, μ.

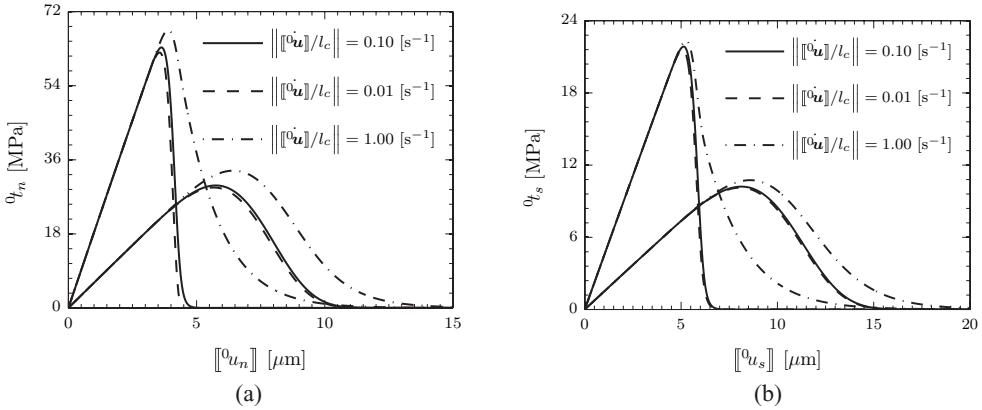

Figure 6. Traction-separation relations for the stiff particle and soft matrix under mixed-mode loading with three different strain-rates. Solid lines denote the strain rate prescribed in subsequent studies, while dashed and dot-dashed lines represent response from 1/10 $\times$ and 10 $\times$ the applied strain rate. Note that the materials are only weakly rate-sensitive over a wide range of strain rates. Also note that the layer thickness in our examples is 200 μm for displacement jump to strain conversion. (a) Normal component of mixed-mode response. (b) Shear component of mixed-mode response.

In this work, we use surrogate material properties given in table 2 that mimic stiff nylon (Nylon 6) particles embedded in a polyurethane structural adhesive (e.g. 3M$^{\text{TM}}$ Polyurethane Structural Adhesive W1600). We choose hyperelastic properties that are within the range of material response reported in references [68, 69]. Moreover, the damage parameters Y_{in}, p_1 and p_2 are chosen to achieve ultimate strength within the range of reported values [68, 69]. One material property that deserves more discussion is the damage viscosity, μ [s^{-1}]. As mentioned in section 2.4, the damage viscosity is inverse proportionally related to the material relaxation time. Unfortunately, in many engineering studies μ is often chosen artificially small, $\mathcal{O}(10^1)$ [27, 45]. This small value allows for easy numerical solution, but results in highly rate-dependent response and unrealistically thick damage zones [27, 28, 45]. In this work, we use $\mu = 100$ s^{-1} which is within the range of reported values for structural adhesives from $\mathcal{O}(10^2)$ to $\mathcal{O}(10^6)$ s^{-1} [70, 71], and results in lower rate-sensitivity and thinner damage zones. The response of each material is shown in figure 6 for three different strain rates. Instead of the typical stress-strain response, we plot the traction-separation relation for easy comparison with multiscale results that follow. We note that the chosen value of μ is on the lower range of physical values. However, the realistic response displayed in figure 6 over the broad range of strain-rates suggests that the selected damage viscosity is acceptable.

4.1. Mesh convergence study

In this section, we determine the required mesh size to capture the hyperelastic, limit (strength), and softening response as well as the fracture toughness. One realization of the cell reconstructed in section 3 with $l_{\text{cell}} \approx l_{\text{stat}}$ is used in this mesh convergence study. The cell contains 93 particles and has dimensions of $139.569 \times 139.569 \times 200\ \mu\text{m}^3$. It is important to note that we use highly unstructured tetrahedral meshes created by the *T3D* meshing tool [72]. The reported mesh size, h, is the desired mesh density and is used as an identifier for the different refinement cases. The meshes have localized refinement and coarsening points which generate finer and coarser elements, but the average element size is guaranteed to be $h_{\text{avg}} \leqslant h$. The average, minimum, and maximum element size, as well as number of nodes, elements, and degrees of freedom (DOFs) are listed in table 3. Note that the finest mesh solved in this work contains over 90 million elements and nearly 48 million nonlinear algebraic equations. Therefore, an efficient solution strategy is essential.

Due to the rate-dependent damage model used in this work, the loading rate has an impact on the mesh convergence. Typically, a slower loading rate will require finer meshes. Recall that a macroscopic loading rate of $\|[\![{}^0\dot{\boldsymbol{u}}]\!]/l_{\text{c}}\| = 0.1\,\text{s}^{-1}$ is used for all simulations, including the mesh convergence study, and that the accuracy of the damage model is controlled by an adaptive time-stepping scheme with $\Delta\omega_{\max} \leqslant 5\%$ (see appendix C). Moreover, to understand the rate effects, figure 6 shows the rate sensitivity of both the matrix and reinforcing particles. Note the small difference in material response for $0.01\ \text{s}^{-1}$ and $0.1\ \text{s}^{-1}$ loading rates. Therefore, the mesh convergence study presented hereafter is sufficiently conclusive for the physical analysis that follows.

Figure 7 shows the macroscopic traction-separation response computed from increasingly finer meshes. Not surprisingly, all discretizations capture the hyperelastic response without any difficulty. Finer meshes transition to a more gradual softening response due to properly capturing the microscale damage features that are linked to morphology and damage properties (e.g. damage viscosity μ). We will analyze these microscale damage features in more detail in subsequent studies (see sections 4.2–4.4).

The convergence of the strength and fracture toughness with respect to decreasing mesh size is displayed in figure 8. We define the dissipated energy (crack driving force—fracture toughness) in the normal and shear directions as

$$G_n = \int_0^{[\![{}^0u_n]\!]_f} {}^0t_n \,\mathrm{d}[\![{}^0u_n]\!] \quad \text{and} \quad G_s = \int_0^{[\![{}^0u_s]\!]_f} {}^0t_s \,\mathrm{d}[\![{}^0u_s]\!], \tag{29}$$

where $[\![{}^0u_n]\!]_f$ and $[\![{}^0u_s]\!]_f$ are the normal and shear values of displacement jump at the final (failure) point in the load history. This normal and shear split is introduced to understand the energy released by the adhesive layer (homogenized RUC) due to the overall normal and shear tractions, respectively. In this work, we combine the in-plane (mode II) and out-of-plane (mode III) shear modes into G_s in accordance with our reduction of shear modes given by equation (28). For the chosen level of mode mixity and applied loading rate (each kept constant throughout the loading process and for all simulations), the computed shear toughness and strength are smaller than their normal counterpart. This trend is observed for all simulations presented in this manuscript, and is likely influenced by the mixed-mode loading conditions as well as the simple isotropic damage model used in this work. Moreover, our kinematic decomposition (see equation (3)) introduces a constraint since the in-plane response of the heterogeneous layer is restricted. Furthermore, similar behavior has been observed experimentally for varying material systems under different levels of mode-mixity (see e.g. [73–76]). A more sophisticated anisotropic damage model could be adopted at the microscale to decouple the normal and shear response [12].

Table 3. Mesh identifiers and characteristics for the grid convergence study.

Identifiers		Characteristics					
h [μm]	$1/h$ [μm^{-1}]	h_{avg} [μm]	h_{min} [μm]	h_{max} [μm]	# nodes	# elements	# DOFs
6.00	0.167	4.34	0.23	8.17	56 809	330 172	167 832
3.00	0.333	2.55	0.16	4.15	307 232	1792 655	913 449
1.50	0.667	1.37	0.073	2.25	2087 736	12 223 528	6232 029
0.75	1.333	0.697	0.022	1.09	16 020 086	93 856 013	47 938 704

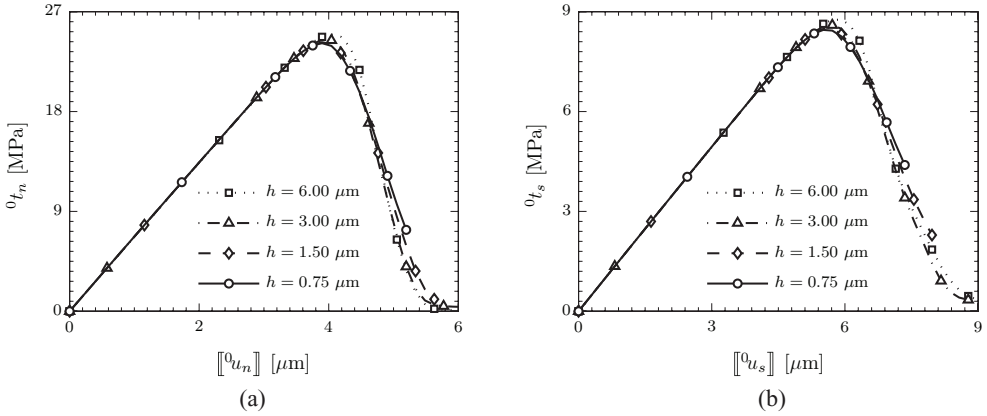

Figure 7. Traction-separation response for selected mesh sizes. (a) Normal component of the mixed-mode response. (b) Shear component of the mixed-mode response.

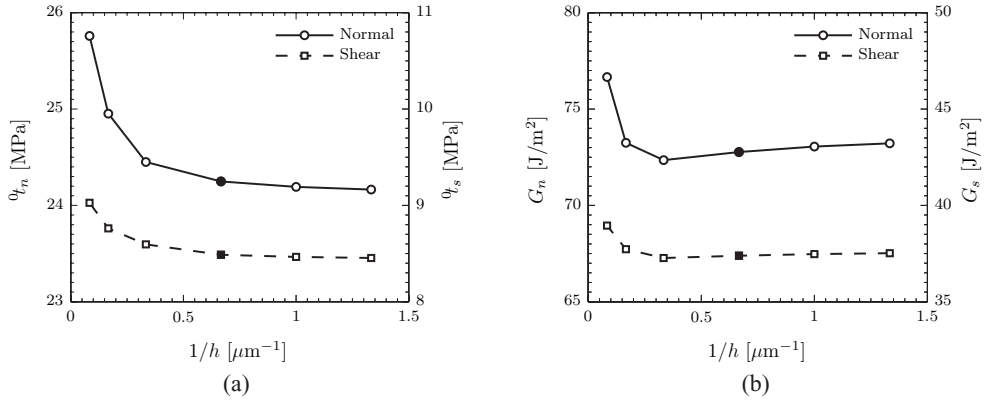

Figure 8. Convergence trend of the macroscopic response with increasing mesh refinement. (a) Convergence trend of strength (maximum traction). (b) Convergence trend of fracture toughness as given by equation (29).

Note that G_n and G_s are different in value from the traditional normal, G_{I}, and shear, G_{II} and/or G_{III}, fracture toughness due to the mixed-mode loading conditions, rate-dependence and finite strain kinematics. In the small strain limit, $G_n \to G_{\text{I}}$ for $[\![^0u_1]\!] = [\![^0u_2]\!] = 0$ and $[\![^0u_3]\!] \neq 0$, while $G_s \to G_{\text{II}}$ for $[\![^0u_2]\!] = [\![^0u_3]\!] = 0$ and $[\![^0u_1]\!] \neq 0$. Similarly, $G_s \to G_{\text{III}}$ for $[\![^0u_1]\!] = [\![^0u_3]\!] = 0$ and $[\![^0u_2]\!] \neq 0$. Under the finite strain kinematics, shear loading introduces a normal opening and

vice versa. The energy release rate, $-Y = {}^{1}\overline{W}$ (see equations (16) and (18)), used in computing the damage surface, equation (19), is an isotropic function of both normal and shear contributions through the Jacobian, J, and deviatoric right Cauchy-Green deformation tensor, $\hat{\boldsymbol{C}}$. Therefore, the total damage dissipation $G_{\text{tot}} = \int_0^{[\![{}^0\boldsymbol{u}]\!]_f} {}^0\boldsymbol{t} \cdot \mathrm{d}[\![{}^0\boldsymbol{u}]\!] \equiv l_c/|\Theta_0| \int_{\Theta_0}\int_0^{t_f} \mathcal{D}^{\omega}\,\mathrm{d}t\,\mathrm{d}\Theta$ is a coupled function of all deformation modes. Note that since we are dealing with heterogeneous materials and isotropy is not strictly enforced, $G_{\text{tot}} \approx G_n + G_s$ in this work.

In this mesh convergence study, we use $\{[\![{}^0u_n]\!]_f, [\![{}^0u_s]\!]_f\} = \{5.20, 7.35\}$ μm for computing the normal and shear fracture toughness. We note that these final normal and shear opening displacements are not those at complete failure (see figure 7). The simulations are prematurely terminated due to convergence issues associated with large mesh distortions. Unfortunately, these convergence issues are common for such large and complex damage simulations (recall that for $h = 0.75$ μm, we solve 47.9 M nonlinear DOFs). A potential solution to these convergence issues can be mesh smoothing or re-discretization (e.g. see [77, 78]). Since we are interested in the numerical properties of the solution (i.e.convergence), we select the last common opening data-point for all mesh densities. This leaves some residual stresses and a portion of the fracture energy is not accounted for. However, we note that neglecting this fraction of energy does not impact the discussion of numerical characteristics since comparisons are made at the same opening displacement. We will comment on this portion of energy in our further studies, where we examine the physics of failure and account for the total fracture toughness.

As seen in figure 8, the strength and fracture toughness converge rapidly and there is a negligible change, from an engineering perspective, for mesh sizes $h \leqslant 1.5$ μm (filled symbols). In order to obtain a higher-order estimate of the continuum response ($h \to 0$), we use Richardson extrapolation [79]. The difference in strength between the estimated continuum response and the mesh with $h = 1.5$ μm is 0.89% for ${}^0t_n$ (${}^0t_n(h \to 0) = 24.04$ MPa) and 1.03% for ${}^0t_s$ (${}^0t_s(h \to 0) = 8.40$ MPa), while the difference in fracture toughness is 0.92% for G_n ($G_n(h \to 0) = 73.44$ J m^{-2}) and 0.59% for G_s ($G_s(h \to 0) = 37.61$ J m^{-2}).

As a final measure of mesh convergence, the damage features are presented for three levels of mesh refinement in figure 9 at the last common loading point (see figure 7). As shown, the coarsest mesh ($h = 3$ μm) does not capture the smaller damage zones and over predicts the level of damage in some regions. The medium and finest meshes ($h = 1.5$ μm and $h = 0.75$ μm) display very similar damage patterns.

In this study, we have shown that resolved behavior of the hyperelastic response, strength, fracture toughness, softening profile (shape of the traction-separation relation), and damage pattern is captured by meshes with average element size $h_{\text{avg}} \leqslant 1.50$ μm. This very fine discretization is primarily required to resolve the thin viscous damage zones, l_μ, resulting from the physical value of the damage viscosity parameter, μ. Based on the small differences in both ${}^0\boldsymbol{t}$ and $G_{n,\,s}$ (maximum error less than 1.05%), we use meshes with $h_{\text{avg}} \leqslant 1.50$ μm for the remainder of this paper. We believe that such a fine mesh density, with $h_{\text{min}} = 0.073$ μm, is essential to properly capture the physics of the problem.

4.2. RUC convergence study

The size of the RUC used in multiscale simulations is key to the computational homogenization framework. In this section, we analyze the material response of three different sized unit cells reconstructed in section 3 (containing 10% volume fraction of 20 μm diameter particles) in order to determine if the geometric length scale also captures the material behavior.

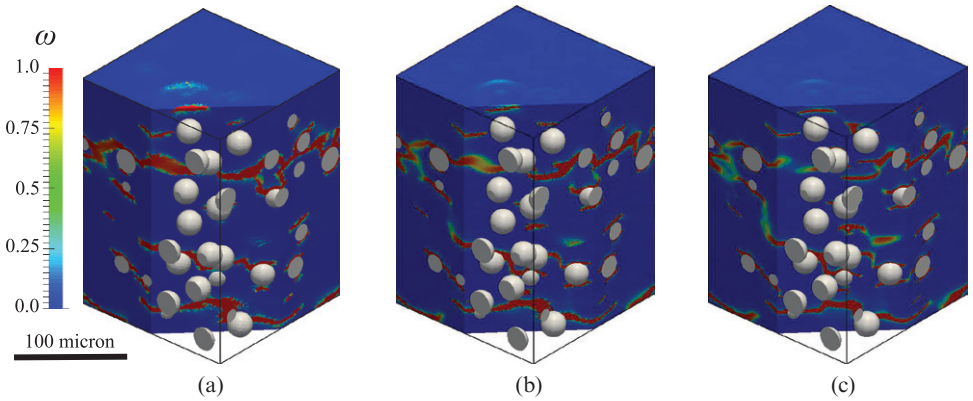

Figure 9. Damage pattern within the microstructure for different levels of mesh refinement. Note that all refinements are shown at the last common point in the load history (see figure 7). (a) $h = 3$ μm. (b) $h = 1.5$ μm. (c) $h = 0.75$ μm.

Table 4. Microstructure and average mesh characteristics for the RUC convergence study.

Cell size	Dimensions [μm^3]	# particles	# nodes	# elements	# DOFs
1/2 l_{stat}	$69.408 \times 69.408 \times 200$	23	552 086	3235 854	1648 686
l_{stat}	$139.569 \times 139.569 \times 200$	93	2103 957	12 317 628	6280 495
2 l_{stat}	$279.887 \times 279.887 \times 200$	374	8294 617	48 537 975	24 758 080

The cells are increasing in size with side lengths $l_{\text{cell}} \approx 1/2\, l_{\text{stat}}$, $l_{\text{cell}} \approx l_{\text{stat}}$, and $l_{\text{cell}} \approx 2\, l_{\text{stat}}$. In what follows, five statistically (macroscopically) equivalent unit cells of different morphology (microstructure) are used, and average response is reported with error bars showing one standard deviation. The dimensions of the cells, number of particles, and the average mesh characteristics for each sized cell are given in table 4.

Figure 10 shows the macroscopic traction-separation response for the different cells. The initial stiffness is identical for each cell, but the limit and softening responses are not. While the two larger unit cells have small and overlapping error bars until the very end of the computed load history (black lines with open symbols), the smallest cell has a distinctly different softening response with very large error. The deviation between the two larger cells at the end of the computed loading history is mostly due to large mesh distortions and the associated deterioration of accuracy, as mentioned previously. Moreover, as in the mesh convergence study, the simulations do not reach complete failure (i.e. $\|{}^0\boldsymbol{t}\| = 0$) due to numerical difficulties. Since we are interested in the complete traction-separation response and the total fracture toughness, we extrapolate the simulation data to failure ($\|{}^0\boldsymbol{t}\| = 0$). Specifically, we linearly extrapolate each independent simulation from the last data-point in the computed load history. The average extrapolated traction-separation relations for each set of five cells (cells with equal side lengths) are displayed as light gray lines with filled markers in figure 10. Note that the average extrapolated data are nonlinear due to the different cell realizations reaching zero traction at different extrapolated opening displacements.

We are interested in the convergence of the maximum traction (strength) and fracture toughness with respect to the side length of the unit cell, l_{cell} (see figure 11). Using the computed and extrapolated data in figure 10, the fracture toughness is evaluated according to equation (29) with $[\![{}^0u_n]\!]_f = [\![{}^0u_s]\!]_f = \infty$. Figure 11 shows the rapid convergence of

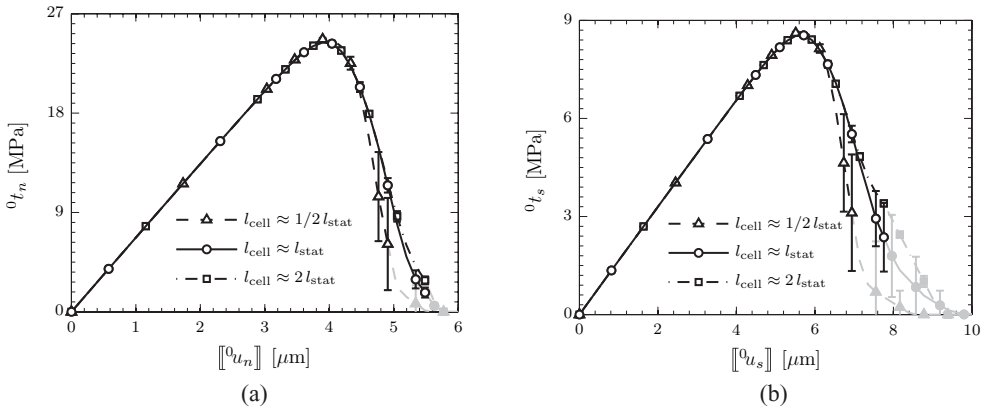

Figure 10. Comparison of the average traction-separation response for different sized cells consisting of 10% volume fraction of 20 μm diameter particles. Error bars represent one standard deviation from five realizations. Average extrapolated simulation data is shown with light gray lines and filled symbols. (a) Normal component of mixed-mode response. (b) Shear component of mixed-mode response.

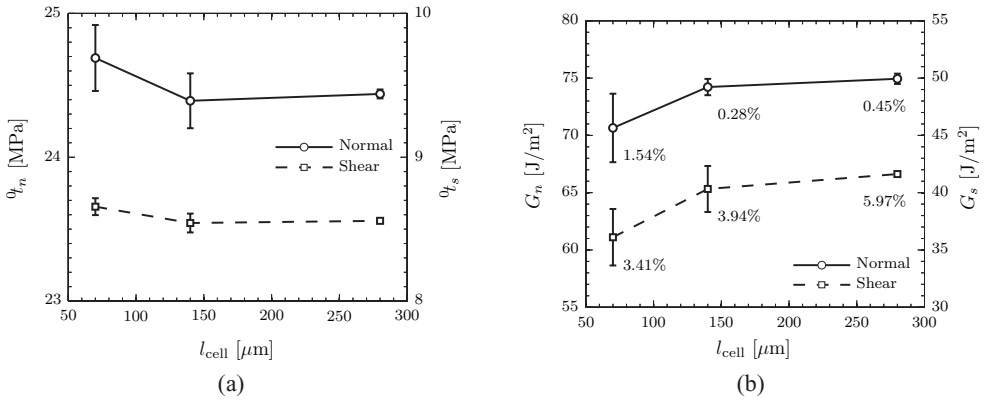

Figure 11. (a) Convergence of strength with increasing cell size. (b) Convergence of fracture toughness with increasing cell size. Percentage values are the contribution of extrapolated data to the mean toughness. Note the diminishing error bars with increasing cell size.

both average and standard deviation of macroscopic response (both strength and fracture toughness) with increasing cell size, using five cell realizations for each cell size. To clearly identify the amount of fracture energy determined from extrapolated data, we report its percentage of the total energy (see figure 11(b)). Note that the maximum contribution of extrapolated data to the average fracture toughness is less than 6.0%. In our previous study [45], rapid convergence of the mean response was also observed. However, the standard deviation of response remained substantial even for very large unit cells. In this study, rapid convergence of both mean and standard deviation can be attributed to the use of statistically equivalent unit cells that attenuate the variation in macroscopic response. The cell with $l_{\text{cell}} \approx 1/2\, l_{\text{stat}}$ (69.408 μm) yields clearly unrepresentative average response with large standard deviation. The cells with $l_{\text{cell}} \approx l_{\text{stat}}$ and $l_{\text{cell}} \approx 2\, l_{\text{stat}}$ have very similar average response with rapidly decaying standard deviation. The reductions in standard deviations are due to

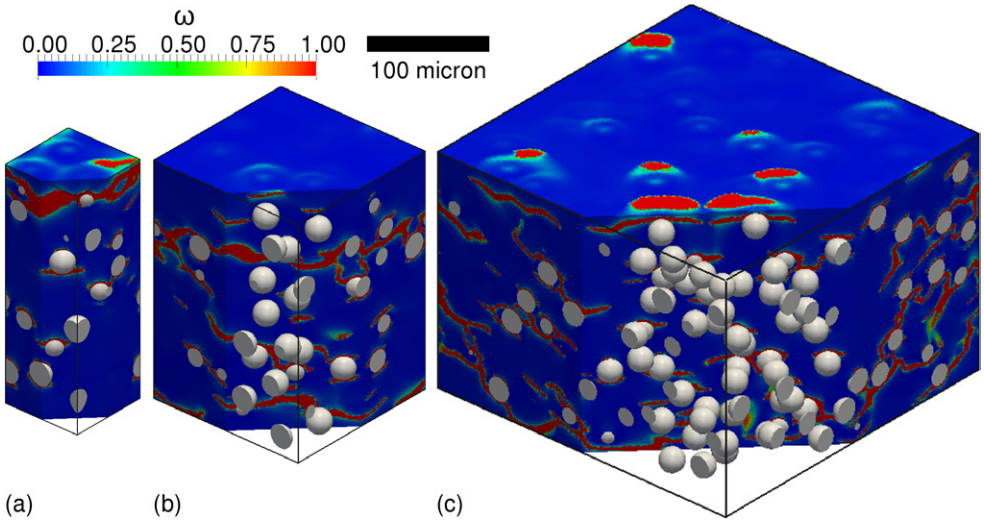

Figure 12. Comparison of the damage pattern at the final computed point in cells with different side lengths. Particles remain undamaged and are colored white for contrast. Only one realization of each sized cell is shown. (a) Failure due to a single dominant crack in a cell with $l_{\text{cell}} \approx 1/2\, l_{\text{stat}}$. (b) Failure due to multiple cracks in a cell with $l_{\text{cell}} \approx l_{\text{stat}}$. (c) Failure due to multiple cracks in a cell with $l_{\text{cell}} \approx 2\, l_{\text{stat}}$.

the larger cells capturing both the geometric (l_{stat}) and physical (l_μ) length scales, including the effect of boundary conditions.

We now compare the damage patterns at the final computed points (last open black symbols in figure 10) for the different sized cells in figure 12. The two larger cells have a more-distributed damage pattern, whereas the cell with $l_{\text{cell}} \approx 1/2\, l_{\text{stat}}$ has a single dominant crack at the top of the cell.

In order to quantify the complex microstructural damage, we introduce two damage metrics. To motivate these metrics, let us consider a single crack of finite thickness, l_μ, with the volume, $V|_\omega$, consisting of points with ω greater or equal to some threshold value as shown in figure 13(a). First, we define

$$M_1|_\omega = \frac{V|_\omega}{V_{\text{cell}}} \quad [-], \tag{30}$$

which is the volume fraction of damage in the microstructure, where V_{cell} is the volume of the cell. Now let us consider a single discrete crack, as shown in figure 13(b), given by the contour of points with ω equal to some threshold value. Similarly to equation (30), we define the damage metric

$$M_2|_\omega = \frac{A|_\omega}{V_{\text{cell}}} \quad [\text{m}^{-1}], \tag{31}$$

which is the area density of cracks in the microstructure for a given value of ω. Note that $A|_\omega$ is the area of only one face of the crack, i.e. $A|_\omega = 1/2\, \partial V|_\omega$, where $\partial V|_\omega$ is the outer surface bounding $V|_\omega$. The damage metrics M_1 and M_2 are related through the effective crack thickness l_μ by

$$l_\mu|_\omega = \left.\frac{M_1}{M_2}\right|_\omega = \left.\frac{V}{A}\right|_\omega \quad [\text{m}]. \tag{32}$$

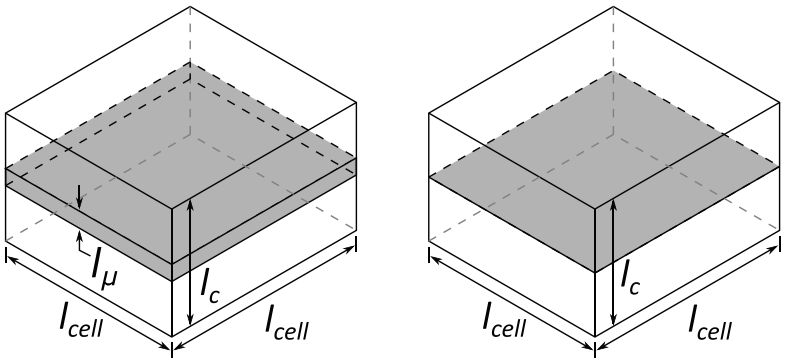

(a) (b)

Figure 13. Schematic of damage metrics for a single dominant crack in the microstructure. For the single damage zone, $M_1 = l_\mu/l_c$ from equation (30) and $M_2 = 1/l_c\ \mathrm{m}^{-1}$ from equation (31). (a) A crack of finite thickness l_μ. (b) A discrete crack face where $\omega = 1$.

Finally, we establish the bounds on M_1 and l_μ, with M_2 being an auxiliary metric only. M_1 is a volume fraction and thus its range is given by $M_1 \in [0, 1]$. At failure, $M_1|_{\omega=1} = 0$ since only the surface of a crack (i.e. no volume) can reach $\omega = 1$. For the case of constant failure throughout the cell (e.g. failure of a cell with $c_\mathrm{p} = 0\%$), $\nabla_{\boldsymbol{Y}}\omega = \boldsymbol{0}\ \forall\, \boldsymbol{Y}$ and $M_1|_\omega = 1$ for any threshold value $\omega \leqslant \omega_{\max}$. Examining equation (32), it is clear that the limit cases for l_μ are given by the limit cases of $V|_\omega = 0$ and $V|_\omega = V_{\mathrm{cell}}$. We note that $V|_\omega \to 0$ faster than $A|_\omega \to 0$, and thus the minimum value of l_μ is 0. In the case that $V_\omega = V_{\mathrm{cell}}$ we get,

$$l_\mu = \frac{l_\mathrm{c}\, l_{\mathrm{cell}}^2}{2l_\mathrm{c}\, l_{\mathrm{cell}} + l_{\mathrm{cell}}^2} + l_\mathrm{c} - l_\mathrm{c} = l_\mathrm{c} - \frac{2l_\mathrm{c}^2}{2l_\mathrm{c} + l_{\mathrm{cell}}}. \tag{33}$$

The periodic boundary conditions approximate $l_{\mathrm{cell}} \to \infty$, and after taking the limit of equation (33) we obtain $l_\mu \in [0, l_\mathrm{c}]$. The effective crack thickness, l_μ, is a macroscopic measure that is related to the material properties (e.g. damage viscosity μ) and the material morphology. The metric M_1 describes the extent of failure in the microstructrue, whereas l_μ characterizes the overall shape of cracks in the microstructure. These metrics allow for quantitative comparison of the microstructural failure between material layers with different morphologies.

Figure 14 shows the volume fraction of damage (M_1) and effective crack thickness (l_μ) for different values of ω at the last computed point (see last black open symbols in figure 10). Note that we plot the damage metrics on the x-axis, since the shape of the curve can be interpreted as the effective crack profile. As can be observed, the damage metrics in the two larger cells are nearly identical, while the smallest cell has a smaller volume fraction of thinner cracks. Additionally, the error bars (one standard deviation) in both M_1 and l_μ are largest for the smallest cell.

With these results, we have established the convergent behavior of both the macroscale properties and our newly defined damage metrics, which encompass the microscopic effects, with respect to the cell size. Furthermore, we have shown that cells that are smaller than the statistically representative cells ($l_{\mathrm{cell}} < l_{\mathrm{stat}}$) are incapable of providing overall material response. While cells with $l_{\mathrm{cell}} \geqslant l_{\mathrm{stat}}$ provide a more accurate and precise material description, they are computationally expensive. Thus, an engineer needs to balance the required accuracy of overall macroscpic response with resulting increases in computational cost. Since

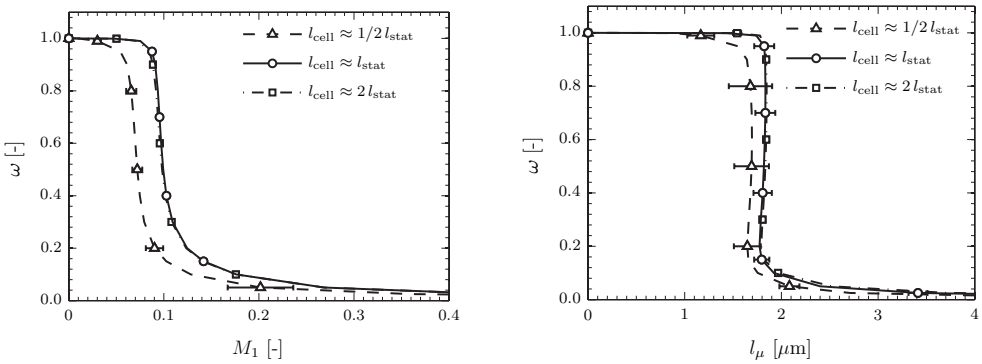

Figure 14. Comparison of damage metrics at the last computed point for different sized unit cells. The standard deviations are shown at the marked points for five realizations of each cell. (a) Volume fraction of damage, M_1. (b) Effective crack thickness, l_μ.

Table 5. Microstructure and average mesh characteristics for the volume fraction study.

c_p	Dimensions [μm^3]	# particles	# nodes	# elements	# DOFs
$0\%^+$	$139.569 \times 139.569 \times 200$	0	1869 193	11 001 473	5577 588
5%	$119.271 \times 119.271 \times 200$	34	1470 546	8619 897	4389 665
10%	$139.569 \times 139.569 \times 200$	93	2103 957	12 317 628	6280 495
20%	$199.766 \times 199.766 \times 200$	381	4588 885	26 843 933	13 699 649

acceptable response for this particular system is obtained for $l_\text{cell} \approx l_\text{stat}$ (the geometric length scale), we define the side length of a RUC as $l_\text{RUC} = l_\text{cell} \approx l_\text{stat}$. Note that the statistical length scale, l_stat, is dependent upon volume fraction, particle diameter, etc as shown in [59]. This leads to cells of different sizes, l_RUC, based on the material morphology (e.g. volume fraction, particle diameter). Here we establish that statistically equivalent cells are sufficient for analysis of this particulate medium. We will return to this point when we analyze individual results of the particle volume fraction and diameter studies.

Finally, we re-emphasize that the relationship between l_RUC and l_stat is dependent on both the microstructure, and the constituent material properties and their contrast. Therefore, the careful RUC analysis performed in this section should be done for any given material system of interest before the conclusion that $l_\text{RUC} \approx l_\text{stat}$ (i.e. the RUC size is based on morphology) is made.

4.3. Effects of particle volume fraction

In this section, we investigate adhesive layers containing 5%, 10%, and 20% volume fraction of 20 μm diameter particles. Five RUCs of each mixture are reconstructed as described in section 3 using the statistics-based geometric length scale, since we established that $l_\text{RUC} \approx l_\text{stat}$ for our systems of interest. We will reinforce this claim with comparisons of standard deviations reported later in this subsection. The RUC dimensions, number of particles, and average mesh properties for each mixture are given in table 5. The homogeneous layer ($c_\text{p} = 0\%$) and layer with an imperfection ($c_\text{p} = 0\%^+$) are also examined. The imperfection is introduced by setting the damage initiation threshold in a small region around the geometric center of the

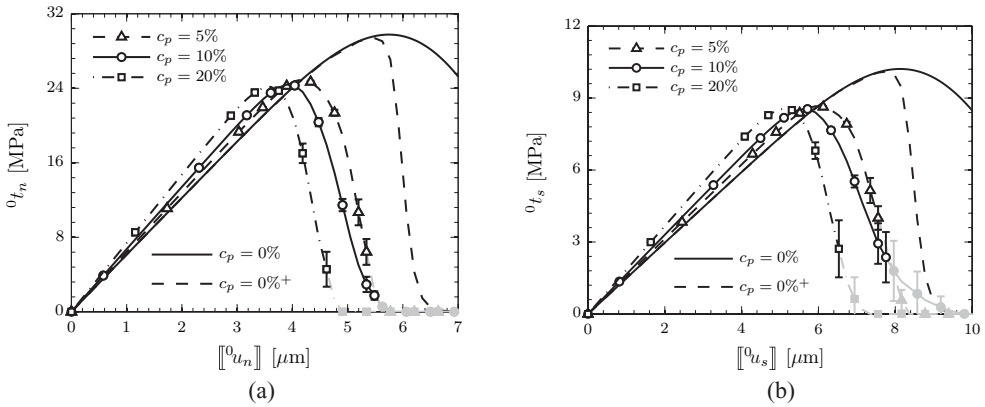

Figure 15. Comparison of average traction-separation response for different volume fraction mixtures of 20 μm diameter particles. The limit cases of homogeneous ($c_\mathrm{p} = 0$ %) and imperfect ($c_\mathrm{p} = 0\%^+$) layers are shown as solid and dashed lines with no symbols. Error bars show one standard deviation of response from five RUCs. Average extrapolated simulation data is shown in light gray with filled symbols. (a) Normal component of the mixed-mode response. (b) Shear component of the mixed-mode response.

layer to a small value, $Y_\mathrm{in} = 10^{-5}$ MPa (compare with Y_in in table 2). We will comment on the effect of the imperfection (strong versus weak) in the next paragraph.

Figure 15 shows the macroscopic traction-separation curves for different volume fraction mixtures. Note again that the light gray lines with filled symbols are average extrapolated data from the final computed points (last open black symbols) to complete failure ($\|{}^0\boldsymbol{t}\| = 0$). We note that the homogeneous and imperfect layers ($c_\mathrm{p} = 0\%$ and $c_\mathrm{p} = 0\%^+$) differ from each other in their failure response. This is because the homogeneous layer damages uniformly (constant failure, $\nabla_{\boldsymbol{Y}}\omega = \boldsymbol{0}\ \forall\, \boldsymbol{Y}$ and $M_\mathrm{I}|_\omega = 1$) with zero microscale displacement fluctuations, and is therefore equivalent to the Taylor estimate described in section 2.3. Conversely, the imperfect layer localizes deformation to a single crack and develops a periodic fluctuation field (see figure 17(a)). The thickness of the localized crack, characterized by l_μ, is influenced by the strength of the defect (imperfection). A weak imperfection results in a thicker crack, whereas a strong imperfection leads to a thinner crack. For very strong imperfections, the thickness of the crack, l_μ, is governed solely by the material properties. We note that there are an infinite number of solutions between the imperfect and homogeneous response depending on the strength of the defect, bounded by l_μ from below (strong imperfection) and l_c from above (weak/no imperfection). We will present the value of l_μ for the matrix later in this section. As l_μ approaches l_c, the homogeneous and imperfect response will become identical as the effect of the imperfection and boundary conditions (homogeneous versus periodic) diminishes.

For the particle reinforced RUCs, we observe that an increase in volume fraction results in increased stiffness, but reduced strength in both normal and shear (figure 15). The 20% volume fraction mixture (dot-dashed line with squares) exhibits steeper softening response in shear due to increased adhesive failure (see also figure 17(d)). We note that the residual tractions of the different mixtures vary (last open symbols on black lines in figure 15). The simulations are terminated at different levels of applied displacement jumps due to numerical difficulties associated with large mesh distortions in the complex damage zones. We comment on these residual tractions as they will become a point of interest in later analysis of the microscale failure.

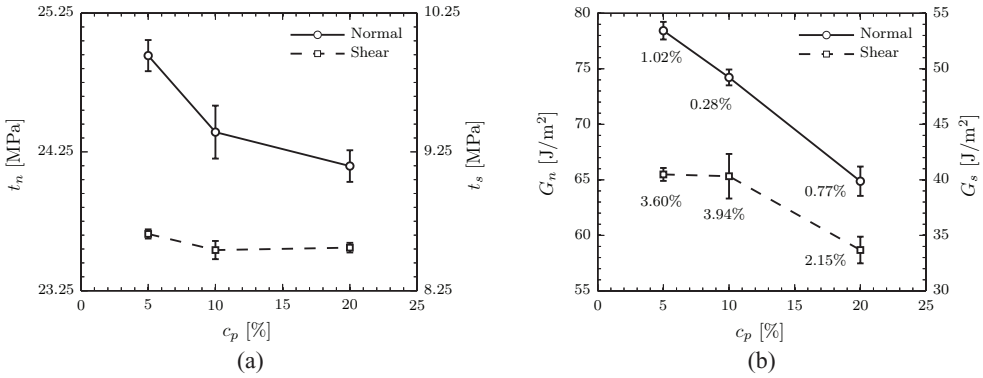

Figure 16. Comparison of strength and fracture toughness for different volume fractions of 20 μm diameter particles. Average and standard deviations are shown for five RUCs of each mixture. (a) Decay of strength with increasing volume fraction. (b) Monotonic decay of fracture toughness with increasing volume fraction. Percentages represent the contribution of extrapolated data to the mean toughness.

Table 6. Strength and fracture toughness for homogeneous and imperfect layers of the matrix material.

c_p	${}^0t_n$ [MPa]	${}^0t_s$ [MPa]	G_n [J m^{-2}]	G_s [J m^{-2}]
0%	29.76	10.21	168.73	81.87
0%$^+$	29.39	10.10	104.78	51.01

The strength and fracture toughness in normal and shear directions are compared in figure 16. As in the previous section, we evaluate the fracture toughness using the computed and extrapolated data shown in figure 15, and identify the contribution from the extrapolated data to the average fracture toughness in figure 16(b). The fracture toughness is computed according to equation (29) with $[\![{}^0u_n]\!]_f = [\![{}^0u_s]\!]_f = \infty$.

All values monotonically decrease with increasing volume fraction of particles except for t_s. Similar trends of decreasing strength and fracture toughness with increasing volume fraction of particles have been observed in experiments of failure in stiff particle reinforced adhesives [30, 31]. We note that the effect of volume fraction on the strength and fracture toughness is strongly influenced by material properties and their contrast. For example, experiments of stiff epoxy with soft embedded particles showed the opposite effect: increasing fracture toughness with increasing volume fraction of particles [32]. The strength and fracture toughness for the homogeneous and imperfect layers are given in table 6, and are higher than the particle reinforced layers for our choice of material properties.

Figure 17 shows the damage pattern in the RUCs at the final computed point with increasing volume fraction of particles. Note that each cell has a different side length, l_RUC, based on the statistical length scale, l_stat (see also [59]). However, the standard deviations over five cell realizations remain small and comparable in value to those of the base study ($c_\mathrm{p} = 10\%$, $d = 20$ μm, see section 4.2). This reconfirms that $l_\mathrm{RUC} \approx l_\mathrm{stat}$ is a good choice for this material system, since large standard deviations would be apparent for unrepresentative cells (see figures 10 and 11). The homogeneous layer, $c_\mathrm{p} = 0\%$, damages uniformly and is not shown. The addition of a strong imperfection causes a pronounced damage localization (figure 17(a)). The shape of the crack is due to the mixed-mode loading with periodic boundary conditions. The 5% volume fraction RUC (figure 17(b)) shows cohesive failure by a thick dominant crack

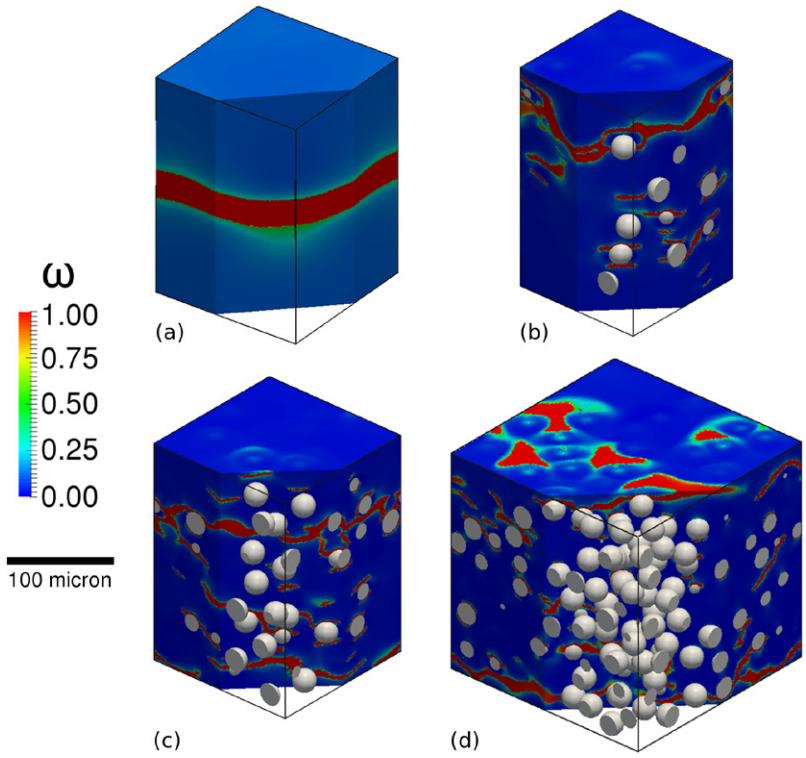

Figure 17. Comparison of the damage pattern at the final computed point in RUCs with increasing volume fractions of 20 μm diameter particles. Particles remain undamaged and are colored white for contrast. Only one realization of each RUC is shown. (a) RUC with a strong imperfection, $c_p = 0\%^+$. (b) RUC with $c_p = 5\%$. (c) RUC with $c_p = 10\%$. (d) RUC with $c_p = 20\%$.

connecting particles in the microstructure. Other small cracks are visible, but they are arrested as a dominant crack is formed. Figure 17(c) shows the damage pattern in the 10% volume fraction RUC. There is still a clear dominant crack, but it is thinner due to the higher number of obstacles. Furthermore, there are large secondary cracks that contribute to material weakening. Finally, figure 17(d) shows the final state of the 20% volume fraction RUC. The damage has localized in cracks towards the top and bottom surfaces, transitioning from cohesive to adhesive failure as particles repel cracks closer to the adherends.

Now we compare the metrics M_1 and l_μ in figure 18 for the range of ω at the final computed point (last black open symbols in figure 15) for the different microstructures. The 5% and 10% volume fraction mixtures have similar volume fractions of damage, but the 10% volume fraction has thinner cracks. The 20% volume fraction mixture has a lower volume fraction of damage, but a similar effective crack thickness as the 10% volume fraction mixture. The effective crack thickness in the higher volume fraction cases is reduced due to the increased number of obstacles and an increased number of thin damage zones mimicking particle debonding (see figures 17(c) and (d)). The larger values of l_μ in the 5% volume fraction case suggest failure due to coalescence of a few thick dominant cracks as opposed to formation of many thin cracks as in the higher volume fraction cases, which is consistent with observations in figure 17. As mentioned previously, the simulations for all volume fraction cases are terminated at different points with varying residual tractions. We note that if all of the mixtures

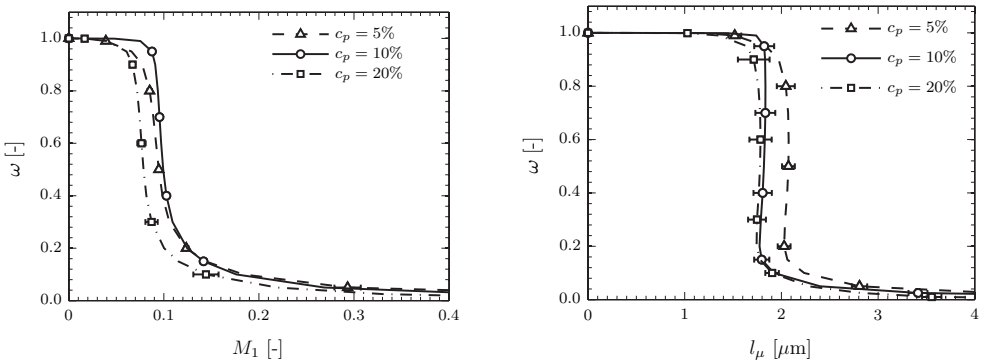

(a) (b)

Figure 18. Comparison of the damage metrics at the final computed point for different volume fraction RUCs. The standard deviations are shown for five realizations of each RUC. (a) Comparison of M_1. (b) Comparison of l_μ.

Table 7. Damage metrics at failure for the homogeneous and imperfect layers. Note that for $c_\mathrm{p} = 0\%$, $l_\mu = l_\mathrm{c} = 200$ μm.

	$M_1\|_{\omega=1/2}$ [-]	$l_\mu\|_{\omega=1/2}$ [μm]
$c_\mathrm{p} = 0\%$	1.0	200
$c_\mathrm{p} = 0\%^+$	0.129	6.702

would be simulated to complete failure ($\|{}^0\boldsymbol{t}\| = 0$), a different trend of M_1 for 5% volume fraction (figure 18(a)) would develop. The 5% volume fraction case (dashed line with triangles) would lie to the right of the 10% volume fraction case (solid line with circles) in figure 18(a). The higher volume fraction of damage is related to additional energy required to break the material, and thus higher fracture toughness as seen in figure 16(b). This trend is consistent with the homogeneous ($c_\mathrm{p} = 0\%$) and imperfect ($c_\mathrm{p} = 0\%^+$) cases (see table 6).

For completeness, the damage metrics of the homogeneous and imperfect layers at failure for $\omega = 1/2$ are given in table 7. Note that the thickness of the crack resulting from the imperfection increases with a weaker defect. We recall that the imperfect layer is made of only the matrix and contains a small but strong defect. Moreover, we point out that increasing the strength of the imperfection ($Y_\mathrm{in} \to 0$) beyond $Y_\mathrm{in} = 10^{-5}$ MPa has no measurable effect on l_μ or the macroscopic response. Thus, for our strong imperfection, $l_\mu|_{\omega=1/2} = 6.702$ μm is the intrinsic crack thickness of the matrix material (see Volokh [24–26]) and is dependent predominantly on the damage parameters (see table 2).

To support the prediction that M_1 at complete failure, $\|{}^0\boldsymbol{t}\| = 0$, would be greater for the 5% case than the 10% case, we examine the evolution of $M_1|_{\omega=1/2}$ and the evolution of the average effective crack thickness. The average effective crack thickness is defined by

$$\overline{l_\mu} = \int_0^1 l_\mu|_\omega \, \mathrm{d}\omega \quad [\mathrm{m}]. \tag{34}$$

A higher volume fraction of particles results in earlier initiation of damage, as depicted in figure 19(a). This early onset of damage leads to a decrease in strength (see figure 16(a)) and is a result of the higher number of damage nucleation sites per unit volume. At the end of the load history in figure 19(a), one can see that the 20% and 10% volume fraction cases

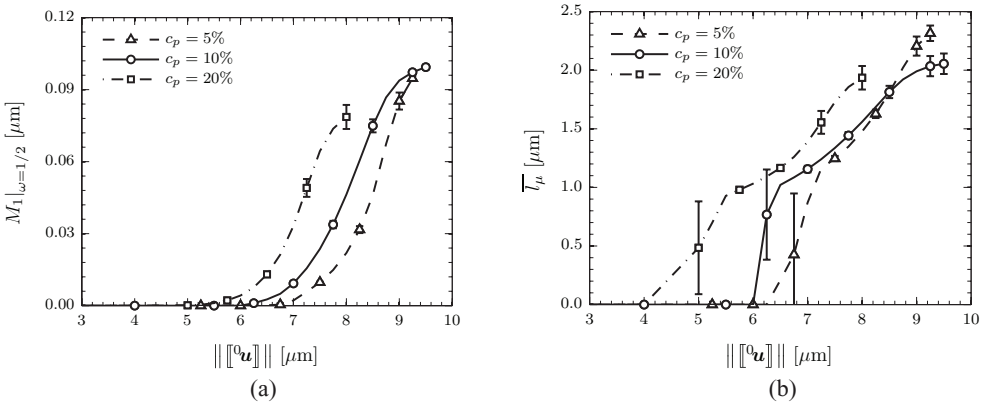

Figure 19. Evolution of damage metrics with respect to $\|[\![^0\boldsymbol{u}]\!]\|$ in RUCs with increasing particle volume fraction. Error bars show one standard deviation for five realizations of each RUC at the marked points. (a) Evolution of M_1 for $\omega = 1/2$. (b) Evolution of $\overline{l_\mu}$ as given in equation (34).

Table 8. Microstructure and average mesh characteristics for the particle diameter study.

d [μm]	Dimensions [μm^3]	# particles	# nodes	# elements	# DOFs
5	$64.982 \times 64.982 \times 200$	1292	1696 876	9836 031	5072 218
10	$99.883 \times 99.883 \times 200$	381	1420 119	8272 851	4242 575
20	$139.569 \times 139.569 \times 200$	93	2103 957	12 317 628	6280 495

are approaching a steady state value of M_1 (the slope of both curves are visibly decreasing), while the 5% volume fraction case is still growing. Although M_1 is still growing, a transition towards the steady-state is slowly beginning for the 5% volume fraction mixture. This continued increase of damaged volume supports our earlier assertion that the 5% line would lie to the right of the 10% line in figure 18(a) at complete failure ($\|^0\boldsymbol{t}\| = 0$). In general, the approach to a steady-state value of M_1 indicates the formation of a connected crack or cracks spanning the entire microstructure. Once such a critical crack pattern is formed, additional crack formation is stopped and ω increases within the existing cracks until failure ($\omega \to 1$). While a dominant crack is clearly visible for the 5% case in figure 17(b), neither M_1 or $\overline{l_\mu}$ have reached a steady state (figure 19) and the microstructure allows the crack thickness to increase before complete failure is reached.

Figure 19(b) shows evolution of the average effective crack thickness, $\overline{l_\mu}$. For all cases, there is rapid growth of the crack thickness as damage is nucleated around particles ($\|[\![^0\boldsymbol{u}]\!]\| \approx 4 - 7\mu$m). Due to the rapid transition from a virgin to damaged state and variations between the RUC realizations, there are large standard deviations in this region. In the 20% volume fraction case (dot-dashed line with squares), there are three easily identifiable growth rate zones excluding the nucleation region. The first zone shows a slow growth in thickness as cracks propagate around and between closely-packed particles. The second zone shows a rapid increase in crack thickness, indicating that the cracks are freely growing in regions with fewer obstacles. Note that the regions with fewest obstacles are near the top and bottom surfaces. Thus, this rapid growth in crack thickness is associated with the transition to adhesive failure (see figure 17(d)). The third zone is the approach to the steady state crack thickness at the end of the

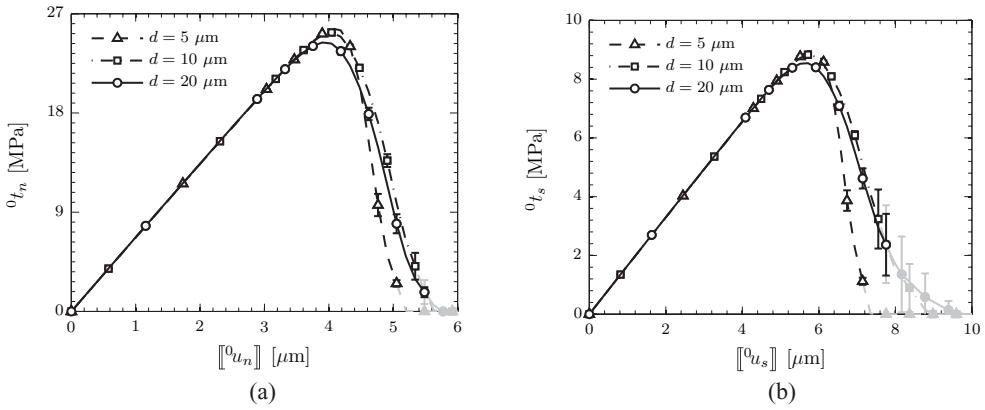

Figure 20. Comparison of traction-separation relations for RUCs with 10% volume fraction of different sized particles. Error bars show one standard deviation of the response for five realizations of each RUC. The light gray lines with filled symbols represent average extrapolated simulation data. (a) Normal component of the mixed-mode response. (b) Shear component of the mixed-mode response.

load history. As with M_1, the approach to a steady state value indicates the development of a dominant crack/cracks in which all further failure occurs (i.e. no new cracks are formed).

These three transition zones, after the nucleation period, are also recognizable in the 10% volume fraction case (solid line with circles) in figure 19(b). However, in this case these three transition zones are more subtle. Zone one shows faster thickness growth than in the 20% case as cracks propagate around and between particles that are farther apart. In the 10% case, there is a smooth transition into zone two, where cracks propagate through the less reinforced binder yet are still being deflected and slowed by particles. In this case, the cracks are not pushed close to the adherends, and the slower growth rate of crack thickness indicates cohesive failure. Finally, the crack thickness approaches the steady-state value in zone three as a network of connected cracks is formed across the microstructure. In the 5% volume fraction case (dashed line with triangles), the sparsely-packed particles allow cracks to propagate with few obstacles. Thus, a nearly constant growth rate in crack thickness is observed after the nucleation period. The crack thickness grows faster, as in the 20% case, since there are fewer obstacles. However, in the 5% case the cracks remain within the material layer and are not repelled to the matrix-rich zones close to the adherends as in the 20% case. At the end of the load history for the 5% case, there is a slight decrease in the growth rate as a dominant crack is being formed.

4.4. Effects of particle diameter

The effects of particle diameter on the macroscopic failure response and microscale failure processes are examined in this section. Five realizations each of RUCs containing 10% volume fraction of 5, 10, and 20 μm diameter particles are reconstructed as described in section 3 using the conjecture that $l_{\text{RUC}} \approx l_{\text{stat}}$ for these particulate composites. The RUC dimensions, number of particles, and average mesh characteristics for each mixture are outlined in table 8.

Figure 20 shows the macroscopic traction-separation relations for each adhesive layer. Again, we extrapolate the traction-separation relations as described in section 4.2 (light gray lines with filled symbols in figure 20). As observed in figure 20, the particle diameter does not affect the hyperelastic response. This has also been observed experimentally for micron

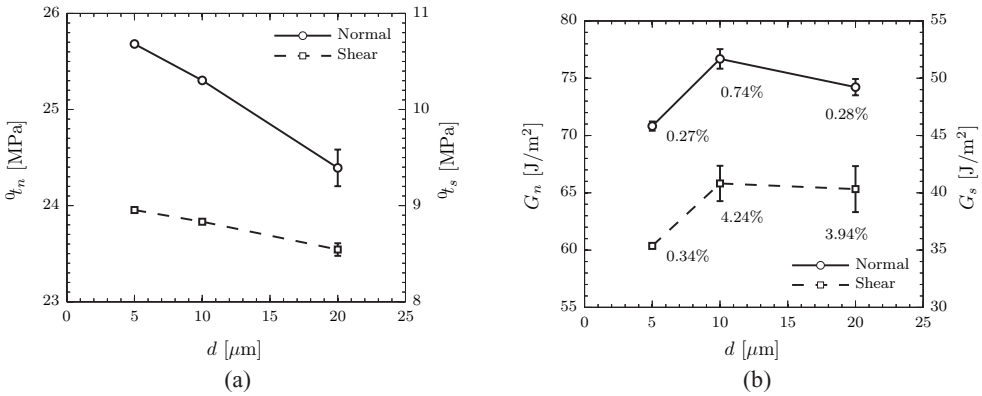

Figure 21. Comparison of strength and fracture toughness for RUCs with 10% volume fraction of different sized particles. Error bars show one standard deviation of response for five RUCs at each marked point. (a) Comparison of strength. (b) Comparison of fracture toughness. The percentages represent the contribution of extrapolated data to the mean toughness.

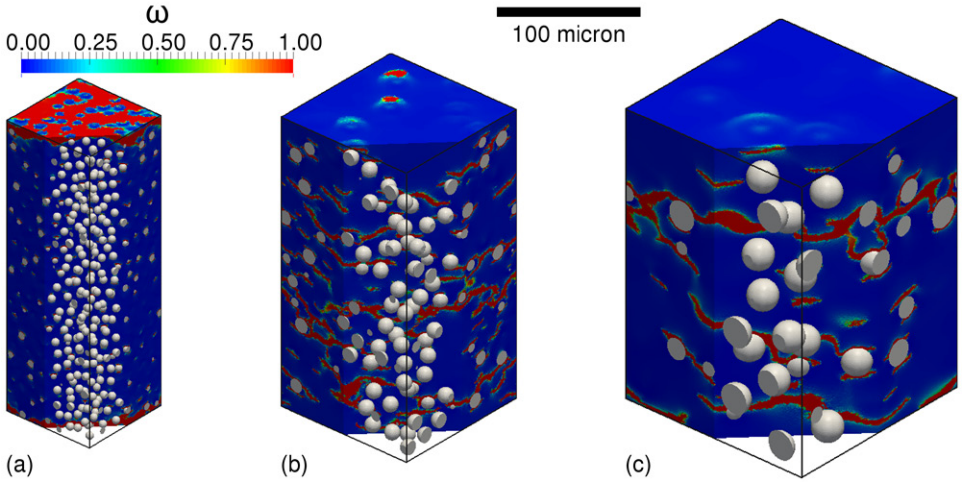

Figure 22. Comparison of the damage pattern at the final computed point for RUCs containing 10% volume fraction of particles with different diameter, d. Only one realization of each RUC is shown. (a) $d = 5$ μm. (b) $d = 10$ μm. (c) $d = 20$ μm.

sized particles [9, 33]. The 5 μm particle mixture shows rapid softening response, particularly in shear, due to the transition to adhesive failure (see figure 22(a)). Figure 21 compares the strength and fracture toughness of the different mixtures. The fracture toughness is computed using equation (29) with $[\![{}^0u_n]\!]_f = [\![{}^0u_s]\!]_f = \infty$. There is a monotonic decrease in the strength with increasing particle diameter, which is often observed in experiments [33, 34]. However, the fracture toughness with relation to particle diameter is non-monotonic and attains a maximum for 10 μm diameter particles. This non-monotonic trend is also observed in experiments for fixed volume fractions [10, 35], and our work shows the ability to capture this particle size effect. We note that the particle size effect is captured because we have sufficiently resolved discretizations ($h_{\min} = 0.073$ μm and $h_{\text{avg}} \leqslant 1.50$ μm), and the value of the damage viscosity,

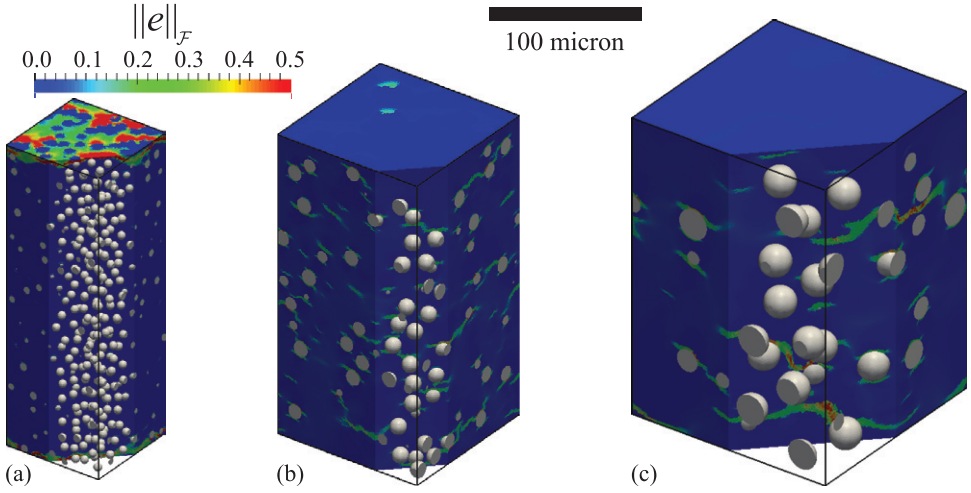

Figure 23. Comparison of the magnitude of the Almansi strain in the different RUCs at the softening inflection point of their respective load histories in figure 20. (a) $d = 5$ μm. (b) $d = 10$ μm. (c) $d = 20$ μm.

μ, is within the range of realistic material properties. Previous numerical studies using a similar damage model were not able to capture the particle size effect due to the highly viscous damage behavior (with thick cracks often on the order of inclusion size) and under resolved computations [27]. Again, note the small standard deviations over five cell realizations in figures 20 and 21. This reinforces our proposition that $l_{\text{RUC}} \approx l_{\text{stat}}$ is a good choice for our studies. The percentage of fracture toughness obtained using the extrapolated data is less than 4.3% (see figure 21(b)).

The damage pattern at the final simulation point for the RUCs with different diameter particles is depicted in figure 22. The 5 μm particle RUC (figure 22(a)) has very small arrested cracks around the particles. The damage localizes at the matrix-rich top and bottom surfaces, leading to adhesive failure. The mixture with 10 μm particles (figure 22(b)) has a well distributed network of thin interconnecting cracks, leading to cohesive failure with multiple dominant cracks. This multiplicity of dominant cracks is very important for increasing fracture toughness. The 20 μm particle mixtures exhibit predominately cohesive failure with fewer dominant cracks.

Figure 23 shows the Frobenius norm of the Almansi strain in the binder for the different RUCs at the inflection point of the softening branch of the load history (see figure 20). As can be seen, the material undergoes large strains ($\sim$50% strains) as it progressively degrades during the damage process (see also the higher strain rate response leading to large failure strains in figure 6). This result shows the importance of the finite strain analysis for damage modeling with progressive softening.

The small volume fraction of damage for the mixture containing 5 μm particles can be observed in figure 24(a). Moreover, there is slightly higher volume fraction of damage in mixtures containing 10 μm particles when compared to the 20 μm mixture. Consistent with the findings in the particle volume fraction study (section 4.3), there is a correlation between increased M_1 at failure and increased fracture toughness (see figure 21(b)).

The effective crack thickness decreases for composites with smaller particles while keeping the volume fraction of particles fixed (see figure 24(b)). As described in section 4.3, the reduction in crack thickness is due to the short inter-particle distance and the increase in thin

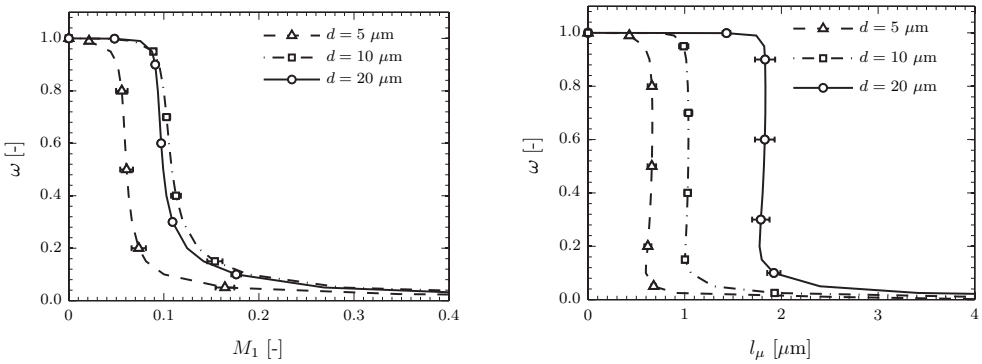

Figure 24. Comparison of damage metrics at the final computed point for RUCs containing 10% volume fraction of different diameter particles. Error bars shown at all marked points represent one standard deviation for five realizations of each RUC. (a) Comparison of M_1. (b) Comparison of l_μ.

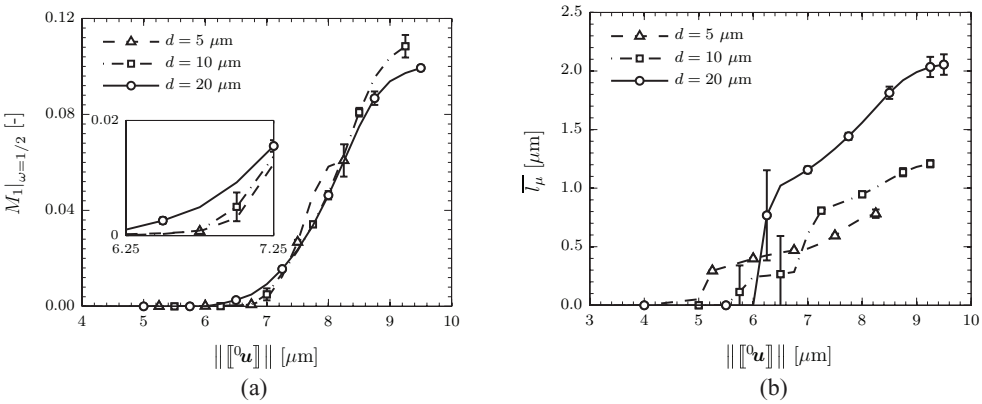

Figure 25. Evolution of damage metrics with respect to $\|[\![^0\boldsymbol{u}]\!]\|$ for RUCs containing 10% of different sized particles. Error bars shown at each marked point represent one standard deviation from five realizations of each mixture. (a) Evolution of M_1 for $\omega = 1/2$. (b) Evolution of $\overline{l_\mu}$.

damage zones around particles, mimicking debonding. Examining figure 24, the small volume fraction of very thin cracks in the 5 μm particle mixture is indicative of strong damage localization, such as in the adhesive failure shown in figure 22(a). The 10 μm particle mixture has the highest volume fraction of thin cracks (see figure 24), suggesting that it has the most-distributed damage pattern (see figure 22(b)). Moreover, a large portion of those cracks are dominant and dissipate a large amount of energy.

The inset in figure 25(a) shows that RUCs containing larger particles accumulate higher volume fractions of damage, M_1, in the early stages after nucleation. This higher amount of damage accounts for the reduction in strength for larger particle diameters (figure 21(a)). Note that while the larger particle RUCs accumulate more damage earlier, the growth rate of M_1 is higher for smaller particle RUCs after the initial damage period (see figure 25(a), $\|[\![^0\boldsymbol{u}]\!]\| > 7.4\ \mu$m). As seen in figure 25(a), RUCs with 5 μm particles have the fastest growth rate and quickly reach a steady-state value of M_1. This rapid growth and approach to a steady-state is indicative

of strong damage localization as in adhesive failure (see figure 22(a)). The 10 μm mixture has a slightly faster growth rate and a slower approach to the steady-state value of M_1 than the 20 μm particle mixture. The faster growth and slower approach to the steady-state value of M_1, in the 10 μm case, suggests that more cracks are being propagated rather than coalescing into a dominant crack.

The distinct evolutions of crack thickness for RUCs containing different sized particles are displayed in figure 25(b). RUCs with smaller particles initiate cracks earlier due to the large number of nucleation sites per unit volume. After this initiation zone, the growth rate for 5 μm particle cells is nearly constant and is the slowest for all mixtures. This is due to the very high density of obstacles that slow crack propagation and force crack formation close to the adherends in relatively matrix-rich regions. In figure 25(b), the 10 μm case shows a three-part evolution of $\overline{l_\mu}$ after the initiation zone ($\|[\![^0\boldsymbol{u}]\!]\| \gtrsim 6$ μm). After initiation, the damage zones mimicking debonding around particles slowly thicken. At $\|[\![^0\boldsymbol{u}]\!]\| \approx 6.8$ μm, there is another rapid growth in crack thickness as cracks propagate into the binder. After this secondary increase, the growth rate is again reduced as cracks propagate between particles. The slow and nearly constant growth rate of $\overline{l_\mu}$ at the end of loading shows that cracks are continually being thinned and deflected by the closely packed particles. This process of thinning and deflecting cracks requires constant energy flux, and thus, the 10 μm system has the highest fracture toughness (see figure 21(b)). Figure 25(b) also displays that RUCs containing 20 μm diameter particles quickly initiate and propagate thick cracks. For the larger particle RUCs, the crack thickness growth rate is faster throughout the loading history since fewer particles deflect and slow the crack formation. Moreover, the 20 μm particles deflect cracks farther from their natural propagation directions (due to the larger particle diameter) and cause larger variations in the crack thickness (see figure 22(c)). When compared to the volume fraction study (figure 19(b)), we see two similar trends in the crack thickness growth rate after nucleation: (i) The density of obstacles (particles) dictates the crack thickness growth rate, with closer-packed systems generally slowing the crack thickness growth. (ii) When the failure pattern is simple, such as with a single dominant crack or adhesive failure, the crack thickness growth rate remains nearly constant.

5. Conclusions

A 3D high-performance finite strain multiscale cohesive framework is used to study failure processes occurring at the microscale in heterogeneous adhesives, and their effect on the macroscopic homogenized cohesive response. An emphasis is placed on data-driven (image-based) modeling that resolves the wide range of spatial scales ($l_\mu \rightarrow l_{\text{RUC}}$). This wide range of spatial scales, consisting of tens of millions of computational cells and millions of highly nonlinear equations, necessitates an efficient solution strategy. We employ parallel computing and execute our framework on up to 1024 computing cores. The large amount of data generated during these simulations requires data-mining and analysis tools to understand the damage patterns and their evolution. Therefore, we propose two damage metrics (i.e. volume fraction of damage and effective crack thickness) that allow us to quantify the damage extent and its evolution. The proposed damage metrics can also serve to catalog materials since they relate the microstructure to overall failure characteristics, such as adhesive versus cohesive failure, strength, and fracture toughness.

In addition, we construct statistically Representative Unit Cells of heterogeneous layers, and their representativeness is studied in terms of hyperelastic response, strength (limit traction), fracture toughness, and softening response (shape of the cohesive relation). The unit

cell reconstruction procedure takes advantage of in-plane isotropic first- and second-order probability functions that are obtained from an image-based source. We show that statistically optimal unit cells yield statistically improved material representation in the L_2 sense than material-blind packing algorithms such as random sequential addition. This leads to smaller standard deviations for physical quantities as compared to previous studies.

Finally, we perform detailed computational studies to understand the effect of volume fraction and particle diameter on micro- and macro-failure characteristics. Our results are statistical in nature, and we present both the means and standard deviations over each set of five material realizations. We capture traditional trends that are observed in experiments, such as the stiffening effect due to the higher particle volume fraction. Additionally, we capture an elusive non-monotonic size-effect in fracture toughness as a function of particle diameter.

Well resolved and verified microscale simulations presented in this work, can be the first step towards virtual materials testing. However, for simulations of this kind to reach their true predictive potential, careful model calibration at the microscale, and detailed model validation both at the micro- and macro-scale must be performed. Moreover, more complex constitutive models (i.e. anisotropic damage) and added physics (e.g. particle-matrix decohesion) are required. Thus, research in co-designed simulations and experiments is the natural next step.

Acknowledgments

This work was supported by the National Science Foundation under Grant Number CMMI-1153435.

Appendix A. Finite element implementation

In our work, the continuum equations are solved using the displacement-based finite element method. We implement the finite element method in a highly parallel computing environment. We use our in-house parallel multiscale code, *PGFem3D*, that has been extensively verified and validated for a variety of problems [50, 66, 67]. The microscale domain is discretized into ${}^1Ne$ convex non-overlapping elements $\Theta^e \subset \mathbb{R}^3$. The microscale displacement field and its gradient are approximated within each element as

$$ {}^1\boldsymbol{u}^h = \sum_{a}^{nn\in\Theta^e} {}^1\tilde{\boldsymbol{N}}_a \, {}^1\boldsymbol{u}_a \quad \text{and} \quad \nabla_{\boldsymbol{Y}} \, {}^1\boldsymbol{u}^h = \sum_{a}^{nn\in\Theta^e} {}^1\tilde{\boldsymbol{B}}_a \, {}^1\boldsymbol{u}_a. \tag{A.1} $$

In equation (A.1), nn is the number of nodes in the element, and ${}^1\boldsymbol{u}_a$ are microscale displacements at node a. ${}^1\tilde{\boldsymbol{N}}_a$ are the shape functions associated with node a satisfying the partition of unity, and ${}^1\tilde{\boldsymbol{B}}_a$ is the discrete gradient operator associated with node a. In this work, we use linear tetrahedral elements.

The discrete weak form of the microscale equilibrium (equation (11)) is given by

$$ \boldsymbol{R} := \frac{l_c}{|\Theta_0|} \mathop{\mathbf{A}}_{e=1}^{{}^1Ne} \int_{\Theta^e} {}^1\boldsymbol{S} : [\boldsymbol{F}^{\mathrm{T}} \, {}^1\tilde{\boldsymbol{B}}]^{\mathrm{sym}} \, \mathrm{d}\Theta = \boldsymbol{0}, \tag{A.2} $$

where $\mathbf{A}$ is the global matrix/vector assembly operator. The discrete form of the traction closure (equation (14)) is given by

$$ {}^0\boldsymbol{t} = \frac{1}{|\Theta_0|} \mathop{\mathbf{A}}_{e=1}^{{}^1Ne} \left\{ \int_{\Theta^e} \boldsymbol{F} \, {}^1\boldsymbol{S} \, \mathrm{d}\Theta \right\} \cdot {}^0\boldsymbol{N}. \tag{A.3} $$

The finite element formulation contains both geometric and material nonlinearity. The solution to the resulting system of nonlinear equations is obtained using Newton's method which requires the discrete tangent operator for optimal iterative convergence. Note that more complex solution paths, such as snap-through and/or snap-back, will require the use of an arc-length method [67, 80]. The convergence criterion in this work is given by $\|\boldsymbol{R}\|/\|\boldsymbol{R}_0\| \leqslant 10^{-5}$, where $\boldsymbol{R}_0 = \boldsymbol{R}(t=0)$ from equation (A.2). The discrete tangent is obtained by linearizing equation (A.2) with respect to $\Delta^1\boldsymbol{u}$, and reads

$$\boldsymbol{K} = \frac{l_c}{|\Theta_0|}\mathop{\mathbf{A}}_{e=1}^{^1Ne}\left\{\int_{\Theta_0} {}^1\boldsymbol{S} : [{}^1\widetilde{\boldsymbol{B}}^{T1}\widetilde{\boldsymbol{B}}]^{\mathrm{sym}}\,\mathrm{d}\Theta + \int_{\Theta_0} [\boldsymbol{F}^{T1}\widetilde{\boldsymbol{B}}]^{\mathrm{sym}} : {}^1\mathbb{L} : [\boldsymbol{F}^{T1}\widetilde{\boldsymbol{B}}]^{\mathrm{sym}}\,\mathrm{d}\Theta\right\}. \tag{A.4}$$

In equation (A.4), ${}^1\mathbb{L}$ is the consistent tangent modulus at the microscale, ${}^1\mathbb{L} = 2\partial^1\boldsymbol{S}/\partial\boldsymbol{C}$. The form of the material tangent modulus for the isotropic damage model is derived in appendix B.

In order to efficiently solve and analyze large computational domains, we have developed a parallel computation and visualization/post-processing framework using the Message Passing Interface (MPI). First, we decompose the mesh generated by *T3D* [72] into domains using a graph partitioning algorithm (*METIS* [81]). Then, within *PGFem3D*, we assign displacement DOFs with both local (domain-specific) and global (solution-specific) identifiers to each node. Next, we construct efficient local-to-global and global-to-local DOF mappings. The mappings are used to define efficient point-to-point non-blocking communication structures for assembling the global system of equations (equations (A.2) and (A.4)) and distributing the updated solution vector. The global system of equations is solved using the *HYPRE* parallel solver library [82]. The error tolerance for the iterative solution (using the generalized minimal residual method) of the linear algebraic equations is 10^{-5}. The simulations produce a large amount of data ($\mathcal{O}(100)$ GB for a single RUC load history in compressed binary format), and efficient post-processing and visualization must also be performed in parallel. We use *ParaView* [83], for parallel visualization and batch data-processing.

Appendix B. Computational damage model

In order to maintain optimal convergence of Newton's algorithm, we derive the instantaneous material tangent, ${}^1\mathbb{L}$, from the discrete evolution equations. In this work, a fully implicit integration algorithm is employed and the discrete damage evolution equations are derived from the first-order Taylor series expansion of equation (22). Assuming $g > 0$ (see equation (19)), the discrete evolution equations are given by

$$\begin{aligned}\omega_{n+1} &= \omega_n + \frac{\Delta t\,\mu}{1+\Delta t\,\mu}[G(\overline{Y}_{n+1}) - \chi_n],\\ \chi_{n+1} &= \frac{\chi_n + \Delta t\,\mu\,G(\overline{Y}_{n+1})}{1+\Delta t\,\mu},\end{aligned} \tag{B.1}$$

where $\Delta t = t_{n+1} - t_n$ is the time increment. The stress update reads

$${}^1\boldsymbol{S}_{n+1} = (1-\omega_{n+1})2\frac{\partial^1\overline{W}}{\partial\boldsymbol{C}}\bigg|_{n+1} = (1-\omega_{n+1})^1\overline{\boldsymbol{S}}_{n+1}. \tag{B.2}$$

The instantaneous material tangent, ${}^1\mathbb{L} = 2\partial^1\boldsymbol{S}/\partial\boldsymbol{C}$, is derived by taking the derivative of equation (B.2), which by the chain rule (recalling that $\overline{Y} = {}^1\overline{W}$) yields

$$
\begin{aligned}
{}^{1}\mathbb{L} &= (1-\omega)2\frac{\partial {}^{1}\overline{\boldsymbol{S}}}{\partial \boldsymbol{C}} - {}^{1}\overline{\boldsymbol{S}}\frac{\partial \omega}{\partial G(\overline{Y})}\frac{\partial G(\overline{Y})}{\partial \overline{Y}}2\frac{\partial \overline{Y}}{\partial \boldsymbol{C}} \\
&= \quad (1-\omega){}^{1}\overline{\mathbb{L}} - \frac{\Delta t\ \mu}{1+\Delta t\ \mu}H[{}^{1}\overline{\boldsymbol{S}} \otimes {}^{1}\overline{\boldsymbol{S}}],
\end{aligned}
\tag{B.3}
$$

where ${}^{1}\overline{\mathbb{L}} = 2\partial {}^{1}\overline{\boldsymbol{S}}/\partial \boldsymbol{C} = 4\partial^{2}\,{}^{1}\overline{W}/\partial \boldsymbol{C}^{2}$ is the hyperelastic material tangent. The damage integration scheme is executed after every linear solve in a nonlinear iterative solution procedure. The accuracy of time integration of the rate-dependent damage model is maintained by an adaptive time stepping procedure described in appendix C. Upon successful convergence of the loading step, the damage and internal state variables are updated as $\omega_n \leftarrow \omega_{n+1}$ and $\chi_n \leftarrow \chi_{n+1}$ for all integration points.

Appendix C. Adaptive damage model integration scheme

In order to accurately integrate the rate-dependent damage model, equation (22) and equation (B.1) in discrete form, an adaptive time-stepping scheme is employed as in [27, 45] and described in algorithm 1. The scheme is based on the desired ratio of damage, $\Delta\omega_{\max}/\Delta\omega_{\mathrm{d}} \to 1$, where $\Delta\omega_{\mathrm{d}}$ is a prescribed optimal (desired) change in ω for accurate integration of the damage model and $\Delta\omega_{\max} = \max_{\boldsymbol{Y}\in\Theta_0}(\Delta\omega(\boldsymbol{Y}))$. In this work, we use $\Delta\omega_{\mathrm{d}} = 0.05$. Upon convergence of the nonlinear solution, algorithm 1 is executed to determine if the current step should be recomputed with a smaller time increment or computations should proceed with a new optimal time increment. In both cases, the prescribed load is modified to maintain a constant loading rate. In algorithm 1, $\alpha_{\mathrm{r}} > 1$ is the prescribed maximum value of α to allow the computation to continue to the next step and $\beta < 1$ is an acceleration parameter given by any acceleration scheme. Note that for $\alpha > 1$, the algorithm will automatically decelerate step $n + 1$.

Algorithm 1. Adaptive time integration for accurate integration of the damage model.

Given: Δt_n, $\Delta\omega_{\max}$, $\Delta\omega_{\mathrm{d}}$, $\alpha_{\mathrm{r}} > 1$
Compute $\alpha = \Delta\omega_{\max}/\Delta\omega_{\mathrm{d}}$
if $\alpha \geqslant \alpha_{\mathrm{r}}$ **them**
  Recompute step n with $\Delta t_n = \Delta t_n/\alpha$
else
  switch α **do**
    case $\alpha \leqslant 0.5$
      Compute acceleration parameter $\beta < 1$.
      Compute $\Delta t_{n+1} = \Delta t_n/\beta$
    case $0.5 < \alpha \leqslant 0.8$
      Compute $\Delta t_{n+1} = \Delta t_n/0.8$
    case $0.8 < \alpha$
      Compute $\Delta t_{n+1} = \Delta t_n/\alpha$
    end switch
end if

References

[1] Griffith A A 1921 The phenomena of rupture and flow in solids *Phil. Trans. R. Soc.* A **221** 163–98
[2] Fish J and Yu Q 2001 Multiscale damage modelling for composite materials: theory and computational framework *Int. J. Numer. Methods Eng.* **52** 161–91
[3] Bažant Z P 1986 Mechanics of distributed cracking *Appl. Mech. Rev.* **39** 675–705
[4] Needleman A 1990 An analysis of tensile decohesion along an interface *J. Mech. Phys. Solids* **38** 289–324
[5] Park K, Paulino G H and Roesler J R 2009 A unified potential-based cohesive model of mixed-mode fracture *J. Mech. Phys. Solids* **57** 891–908
[6] Kim D J, Pereira J P and Duarte C A 2010 Analysis of three-dimensional fracture mechanics problems: a two-scale approach using coarse-generalized fem meshes *Int. J. Numer. Methods Eng.* **81** 335–65
[7] Huynh D B P and Belytschko T 2009 The extended finite element method for fracture in composite materials *Int. J. Numer. Methods Eng.* **77** 214–39
[8] Bažant Z P and Jirásek M 2002 Nonlocal integral formulations of plasticity and damage: survey of progress *J. Eng. Mech.* **128** 1119–49
[9] Spanoudakis J and Young R J 1984 Crack propagation in a glass particle-filled epoxy resin *J. Mater. Sci.* **19** 473–86
[10] Kitey R and Tippur H V 2005 Role of particle size and filler—matrix adhesion on dynamic fracture of glass-filled epoxy. I. Macromeasurements *Acta Mater.* **53** 1153–65
[11] Voyiadjis G Z, Al-Rub R K A and Palazotto A N 2004 Thermodynamic framework for coupling of non-local viscoplasticity and non-local anisotropic viscodamage for dynamic localization problems using gradient theory *Int. J. Plast.* **20** 981–1038
[12] Ju J W 1989 Energy-based coupled elastoplastic damage models at finite strains *J. Eng. Mech.* **115** 2507–25
[13] Simo J C and Ju J W 1987 Strain- and stress-based continuum damage models–I. Formulation *Int. J. Solids Struct.* **23** 821–40
[14] Freund L B 1998 *Dynamic Fracture Mechanics* (Cambridge: Cambridge University Press)
[15] Rice J R 1968 A path independent integral and the approximate analysis of strain concentration by notches and cracks *J. Appl. Mech.* **35** 379–86
[16] Irwin G R 1957 Analysis of stresses and strains near the end of a crack traversing a plate *J. Appl. Mech.* **24** 361–4
[17] Willis J R 1967 A comparison of the fracture criteria of griffith and barenblatt *J. Mech. Phys. Solids* **15** 151–62
[18] Buehler M J, Abraham F F and Gao H 2003 Hyperelasticity governs dynamic fracture at a critical length scale *Nature* **426** 141–6
[19] Barenblatt G I 1962 The mathematical theory of equilibrium cracks in brittle fracture *Adv. Appl. Mech.* **7** 55–129
[20] Dugdale D S 1960 Yielding of steel sheets containing slits *J. Mech. Phys. Solids* **8** 100–4
[21] Krajcinovic D 1995 Continuum damage mechanics: when and how? *Int. J. Damage Mech.* **4** 217–29
[22] Kachanov L 1986 *Introduction to Continuum Damage Mechanics* vol 10 (Berlin: Springer)
[23] Xue Z, Pontin M G, Zok F W and Hutchinson J W 2010 Calibration procedures for a computational model of ductile fracture *Eng. Fract. Mech.* **77** 492–509
[24] Volokh K Y 2012 Characteristic length of damage localization in steel *Eng. Fract. Mech.* **94** 85–6
[25] Volokh K Y 2011 Characteristic length of damage localization in rubber *Int. J. Fract.* **168** 113–6
[26] Volokh K Y 2013 Characteristic length of damage localization in concrete *Mech. Res. Commun.* **51** 29–31
[27] Matouš K, Kulkarni M G and Geubelle P H 2008 Multiscale cohesive failure modeling of heterogeneous adhesives *J. Mech. Phys. Solids* **56** 1511–33
[28] Aragón A M, Soghrati S and Geubelle P H 2013 Effect of in-plane deformation on the cohesive failure of heterogeneous adhesives *J. Mech. Phys. Solids* **61** 1600–11
[29] Pearson R A and Yee A F 1991 Influence of particle size and particle size distribution on toughening mechanisms in rubber-modified epoxies *J. Mater. Sci.* **26** 3828–44
[30] Dekkers M E J and Heikens D 1983 The effect of interfacial adhesion on the tensile behavior of polystyrene–glass-bead composites *J. Appl. Polym. Sci.* **28** 3809–15

[31] Huang L, Yuan Q, Jiang W, An L, Jiang S and Li R K Y 2004 Mechanical and thermal properties of glass bead–filled nylon-6 *J. Appl. Polym. Sci.* **94** 1885–90
[32] Kinloch A J and Hunston DL 1987 Effect of volume fraction of dispersed rubbery phase on the toughness of rubber-toughened epoxy polymers *J. Mater. Sci. Lett.* **6** 137–9
[33] Radford K C 1971 The mechanical properties of an epoxy resin with a second phase dispersion *J. Mater. Sci.* **6** 1286–91
[34] Nakamura Y, Yamaguchi M, Okubo M and Matsumoto T 1992 Effects of particle size on mechanical and impact properties of epoxy resin filled with spherical silica *J. Appl. Polym. Sci.* **45** 1281–9
[35] Singh R P, Zhang M and Chan D 2002 Toughening of a brittle thermosetting polymer: effects of reinforcement particle size and volume fraction *J. Mater. Sci.* **37** 781–8
[36] Lee H H, Chou K S and Shih Z W 2005 Effect of nano-sized silver particles on the resistivity of polymeric conductive adhesives *Int. J. Adhes. Adhes.* **25** 437–41
[37] White S R, Sottos N R, Geubelle P H, Moore J S, Kessler M, Sriram S R, Brown E N and Viswanathan S 2001 Autonomic healing of polymer composites *Nature* **409** 794–7
[38] Rijken P and Cooke M L 2001 Role of shale thickness on vertical connectivity of fractures: application of crack-bridging theory to the austin chalk, texas *Tectonophysics* **337** 117–33
[39] Kreger-van Rij N J W and Veenhuis M 1971 A comparative study of the cell wall structure of basidiomycetous and related yeasts *J. Gen. Microbiology* **68** 87–95
[40] Malacarne J, Carvalho R M, de Goes M F, Svizero N, Pashley D H, Tay F R, Yiu C K and de Oliveira Carrilho M R 2006 Water sorption/solubility of dental adhesive resins *Dental Mater.* **22** 973–80
[41] Tayapongsak P, O'Brien D A, Monteiro C B and Arceo-Diaz L Y 1994 Autologous fibrin adhesive in mandibular reconstruction with particulate cancellous bone and marrow *J. Oral Maxillofac. Surg.* **52** 161–5
[42] Ferreira J M, Silva H, Costa J D and Richardson M 2005 Stress analysis of lap joints involving natural fibre reinforced interface layers *Composites* B **36** 1–7
[43] Hsiao K T, Alms J and Advani S G 2003 Use of epoxy/multiwalled carbon nanotubes as adhesives to join graphite fibre reinforced polymer composites *Nanotechnology* **14** 791–3
[44] Hill R 1972 On constitutive macro-variables for heterogeneous solids at finite strain *Proc. R. Soc.* A **326** 131–47
[45] Kulkarni M G, Geubelle P H and Matouš K 2009 Multi-scale modeling of heterogeneous adhesives: effect of particle decohesion *Mech. Mater.* **41** 573–83
[46] Alfaro C, Suiker A S J, Verhoosel C V and De Borst R 2010 Numerical homogenization of cracking processes in thin fibre-epoxy layers *Eur. J. Mech.* A **29** 119–31
[47] Nguyen V P, Lloberas-Valls O, Stroeven M and Sluys L J 2012 Computational homogenization for multiscale crack modeling. Implementational and computational aspects *Int. J. Numer. Methods Eng.* **89** 192–226
[48] Kulkarni M G, Matouš K and Geubelle P H 2010 Coupled multi-scale cohesive modeling of failure in heterogeneous adhesives *Int. J. Numer. Methods Eng.* **84** 916–46
[49] Hirschberger C B, Ricker S, Steinmann P and Sukumar N 2009 Computational multiscale modelling of heterogeneous material layers *Eng. Fract. Mech.* **76** 793–812
[50] Mosby M and Matouš K 2014 Hierarchically parallel coupled finite strain multiscale solver for modeling heterogeneous layers *Int. J. Numer. Methods Eng.* **102** 748–65
[51] Coenen E W C, Kouznetsova V G and Geers M G D 2012 Multi-scale continuous–discontinuous framework for computational-homogenization–localization *J. Mech. Phys. Solids* **60** 1486–507
[52] McBride A, Mergheim J, Javili A, Steinmann P and Bargmann S 2012 Micro-to-macro transitions for heterogeneous material layers accounting for in-plane stretch *J. Mech. Phys. Solids* **60** 1221–39
[53] Adams M F and Taylor R L 2000 Parallel multigrid solvers for 3d unstructured finite element problems in large deformation elasticity and plasticity *Int. J. Numer. Methods Eng.* **48** 1241–62
[54] Khisaeva Z F and Ostoja-Starzewski M 2006 On the size of rve in finite elasticity of random composites *J. Elast.* **85** 153–73
[55] Gitman I M, Askes H and Sluys L J 2007 Representative volume: existence and size determination *Eng. Fract. Mech.* **74** 2518–34
[56] Swaminathan S and Ghosh S 2006 Statistically equivalent representative volume elements for unidirectional composite microstructures: part II-with interfacial debonding *J. Compos. Mater.* **40** 605–21

[57] Lee H, Brandyberry M, Tudor A and Matouš K 2009 Three-dimensional reconstruction of statistically optimal unit cells of polydisperse particulate composites from microtomography *Phys. Rev.* E **80** 061301
[58] Torquato S 2002 *Random Heterogeneous Materials: Microstructure and Macroscopic Properties* vol 16 (Berlin: Springer)
[59] Collins B C, Matous K and Rypl D 2010 Three-dimensional reconstruction of statistically optimal unit cells of multimodal particulate composites *Int. J. Multiscale Comput. Eng.* **8** 489–507
[60] Coleman B D and Noll W 1963 The thermodynamics of elastic materials with heat conduction and viscosity *Arch. Ration. Mech. Anal.* **13** 167–78
[61] Lubliner J 1972 On the thermodynamic foundations of non-linear solid mechanics *Int. J. Nonlinear Mech.* **7** 237–54
[62] O'Brien D J, Mather P T and White S R 2001 Viscoelastic properties of an epoxy resin during cure *J. Compos. Mater.* **35** 883–904
[63] Chen W and Zhou B 1998 Constitutive behavior of epon 828/t-403 at various strain rates *Mech. Time-Dependent Mater.* **2** 103–11
[64] Gillman A, Matouš K and Atkinson S 2013 Microstructure-statistics-property relations of anisotropic polydisperse particulate composites using tomography *Phys. Rev.* E **87** 022208
[65] Lubachevsky B D, Stillinger F H and Pinson E N 1991 Disks versus spheres: contrasting properties of random packings *J. Stat. Phys.* **64** 501–24
[66] Matouš K and Maniatty A M 2004 Finite element formulation for modelling large deformations in elasto-viscoplastic polycrystals *Int. J. Numer. Methods Eng.* **60** 2313–33
[67] Matouš K and Geubelle P H 2006 Multiscale modelling of particle debonding in reinforced elastomers subjected to finite deformations *Int. J. Numer. Methods Eng.* **65** 190–223
[68] Bolton W 2011 *Materials for Engineering* 2nd edn (New York: Routledge)
[69] 2012 3M, 3M^{TM} polyurethane structural adhesive W1600
[70] Karim M R 2005 Constitutive modeling and failure criteria of carbon-fiber reinforced polymers under high strain rates *PhD Thesis* The University of Akron
[71] Argoul P, Benzarti K, Freddi F, Frémond M and Nguyen T-H T 2011 A damage model to predict the durability of bonded assemblies–part II: parameter identification and preliminary results for accelerated ageing tests *Constr. Build. Mater.* **25** 556–67
[72] Bittnar Z and Rypl D 1996 Direct triangulation of 3D surfaces using advancing front technique *Proc. of the 2nd ECCOMAS Conf. on Numerical Methods in Engineering* ed J-A Désidéri *et al* (New York: Wiley) pp 86–90
[73] Seo D W and Lim J K 2005 Tensile, bending and shear strength distributions of adhesive-bonded butt joint specimens *Compos. Sci. Technol.* **65** 1421–7
[74] Meguid S A and Sun Y 2004 On the tensile and shear strength of nano-reinforced composite interfaces *Mater. Des.* **25** 289–96
[75] Zhu Y, Liechti K M and Ravi-Chandar K 2009 Direct extraction of rate-dependent traction–separation laws for polyurea/steel interfaces *Int. J. Solids Struct.* **46** 31–51
[76] Zhou B, Thouless M D and Ward S M 2006 Predicting the failure of ultrasonic spot welds by pull-out from sheet metal *Int. J. Solids Struct.* **43** 7482–500
[77] Brewer M L, Diachin L F, Knupp P M, Leurent T and Melander D J 2003 The mesquite mesh quality improvement toolkit *International Meeting Roundtable*
[78] Freitag L A and Plassmann P *et al* 2000 Local optimization-based simplicial mesh untangling and improvement *Int. J. Numer. Methods Eng.* **49** 109–25
[79] Roache P J 1998 *Verification and Validation in Computational Science and Engineering* (Albuquerque, NM: Hermosa)
[80] Wriggers P and Simo J C 1990 A general procedure for the direct computation of turning and bifurcation points *Int. J. Numer. Methods Eng.* **30** 155–76
[81] Karypis G and Kumar V 1998 A fast and high quality multilevel scheme for partitioning irregular graphs *SIAM J. Sci. Comput.* **20** 359–92
[82] 2012 Center for Applied Scientific Computing, Hypre User's Manual Lawrence Livermore National Laboratory
[83] Squillacote A H 2007 *The ParaView Guide* (New York: Kitware)